Doctoral Thesis in Engineering Mechanics

Neuromechanical Assessment of Intact and Impaired Muscle Control

High-density EMG-informed approach

ASTA KIZYTE

KTH ROYAL INSTITUTE OF TECHNOLOGY

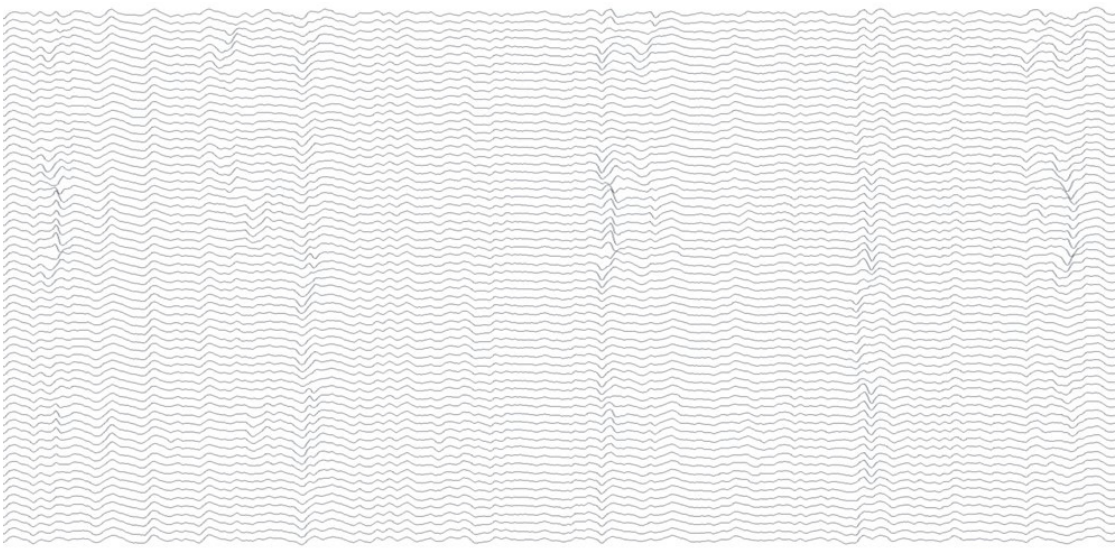

Neuromechanical Assessment of Intact and Impaired Muscle Control

High-density EMG-informed approach

ASTA KIZYTE

Academic Dissertation which, with due permission of the KTH Royal Institute of Technology,
is submitted for public defence for the Degree of Doctor of Philosophy on Friday 23rd of May 2025,
at 9:00 a.m. in Kollegiesalen, Brinellvägen 6, Stockholm.

Doctoral Thesis in Engineering Mechanics
KTH Royal Institute of Technology
Stockholm, Sweden 2025

Cover page photo: High-density electromyography signals of the tibialis anterior muscle

TRITA-SCI-FOU 2025:20
ISBN 978-91-8106-248-9

Printed by: Universitetsservice US-AB, Sweden 2025

Abstract

Neuromuscular impairments in ankle dorsi-/plantarflexor muscles present rehabilitation challenges after spinal cord injury (SCI) and stroke. Reliable torque prediction and characterization of muscle impairments are essential for guiding rehabilitation and monitoring recovery. This thesis aims to assess how high-density EMG (HDEMG) improves torque estimation by integrating spatial and neurophysiological data (Studies I & II) and examine motor unit (MU) behavior and corticomuscular connectivity in SCI and stroke (Studies III & IV).

Proposed methodologies combine HDEMG with advanced signal processing techniques. Specifically, Study I uses machine learning (ML) to predict torque from bipolar EMG, HDEMG, and extracted features. Study II incorporates a computational cumulative spike train-driven motoneuron pool model into a neuromusculoskeletal framework to generate neural drive signals. Study III uses HDEMG decomposition to analyze MU firing behavior in SCI. Study IV investigates MU/EMG–EEG corticomuscular coherence (CMC) to assess corticospinal disruptions in stroke.

Findings from Studies I & II show ML methods predict torque well in static conditions but face challenges in dynamic movement due to absence of kinematic constraints. Neuromusculoskeletal modeling provides better representation of neural and mechanical function by incorporating MU firing properties. Studies III & IV offer insights into MU-level changes in neuromuscular disorders. Specifically, Study III identifies SCI-related EMG and MU behavior alterations, reflecting compensatory motor control strategies. Study IV introduces MU-level CMC analysis in stroke, revealing that motor neuron parameters do not significantly determine CMC strength, and the fundamental pattern of beta-band coupling over motor areas remains identifiable across all subject groups and CMC modalities.

Overall, this thesis demonstrates that HDEMG enhances torque estimation and neuromuscular assessment. By integrating spatial EMG features and MU-level analyses, it deepens understanding of pathological motor control and neurophysiology, with implications for rehabilitation, assistive devices, and neuromuscular modeling.

Keywords
Neuromuscular modeling, torque estimation, machine learning, motor unit, stroke, spinal cord injury

Sammanfattning

Neuromuskulära funktionsnedsättningar i dorsal-/plantarflexor i fotleden utgör stora rehabiliteringsutmaningar efter ryggmärgsskada (RMS) och stroke. Att karakterisera muskel-funktionsnedsättningar är avgörande för att följa upp återhämtning. Tillförlitlig vridmomentestimering är väsentlig för planering av rehabiliteringsstrategier. Denna avhandling syftar till att (i) bedöma hur högdensitets elektromyografi (HDEMG) förbättrar vridmomentestimering genom att integrera rumsliga och neurofysiologiska data (Studie I & II) och (ii) undersöka muskelaktivering och motorenhetsbeteende (ME) hos individer med RMS och stroke (Studie III & IV).

Metodologierna kombinerar HDEMG med avancerad signalbehandling. Studie I använder maskininlärning (ML) för att estimera vridmoment från EMG, HDEMG och EMG-baserade egenskaper. Studie II använder en beräkningsmodell för motoneuronpooler, driven av kumulativt spikmönster (CST), in i ett neuromuskuloskeletalt ramverk för att generera nervsignalstyrka. Studie III använder HDEMG-dekomposition för att analysera ME-avfyrning vid RMS. Studie IV undersöker ME/EMG-EEG corticomuskulär koherens (CMC) för att upptäcka corticospinala störningar hos individer efter stroke.

Resultaten från Studie I och II visar att ML-metoder estimerar vridmoment tillförlitligt under statiska förhållanden men har svårigheter vid dynamiska rörelser på grund av saknande kinematisk information. Neuromuskuloskeletal modellering avbildar bättre motorisk och mekanisk funktion genom att integrera ME-avfyrningsegenskaper. Studie III och IV ger insikter i förändringar på ME-nivå vid neuromuskulära sjukdomar. Studie III identifierar EMG- och ME-förändringar relaterade till RMS. Studie IV visar att motorneuronparameterar inte påverkar CMC-styrka och att det grundläggande beta-bandmönstret är identifierbart i alla CMC-modaliteter.

Sammanfattningsvis visar denna avhandling att HDEMG förbättrar vridmomentestimering och neuromuskulär bedömning. Genom att integrera rumsliga EMG-egenskaper och ME-analyser fördjupas förståelsen för motorstyrning och neurofysiologi, med implicita konsekvenser för rehabilitering, hjälpmedel och modellering.

Nyckelord
Neuromuskulär modellering, vridmomentestimering, maskininlärning, motorenhet, stroke, ryggmärgsskada.

List of publications

This thesis is based on the publications listed below:

Study I: Asta Kizyte, Yuchen Lei, and Ruoli Wang. Influence of Input Features and EMG Type on Ankle Joint Torque Prediction With Support Vector Regression. (Published in *IEEE Transactions on Neural Systems and Rehabilitation Engineering*, vol. 31, pp. 4286-4294, 2023)

Study II: Asta Kizyte, Zhihao Duan, Anton Arndt, Olga Tarassova, and Ruoli Wang. Motor Unit Pool-Driven Modeling Approach for Estimation of Isometric And Isokinetic Ankle Torque. (Manuscript)

Study III: Asta Kizyte, Haocheng Zhang, Emelie Butler Forslund, Elena Gutierrez-Farewik, and Ruoli Wang. Neuromuscular Adaptations in Soleus and Tibialis Anterior Muscles in Persons with Spinal Cord Injury. (Submitted)

Study IV: Asta Kizyte, Hanxun Zhang, Legeng Lin, Xiaoling Hu, Ruoli Wang. Advancing Cortico-muscular Coherence Analysis in Stroke: EEG Coupled with Motor Unit Spike Train Data. (Manuscript)

Author contributions

The main supervisor of the doctoral project is Ruoli Wang, with co-supervision by Elena Gutierrez-Farewik. The division of work between authors of the four studies included in this thesis are presented in table A.

Table A. Authors' contributions to the publications according to the CRediT (Contributor Roles Taxonomy) terminology.

Contribution	Initials of contributing authors			
	Study I	Study II	Study III	Study IV
Conceptualization	RW, AK	AK, RW	AK, EBF, RW, EGF	AK, RW, XH
Data curation	AK, RW	AK, RW	AK, RW, EBF, EGF	AK, HZ
Formal analysis	AK	AK, ZD	AK, HZ	AK, HZ
Funding acquisition	RW	RW	RW, EGF	RW, XH
Investigation	AK, RW	AK, ZD, RW	AK, EBF	AK, HZ, LL
Software	AK, YL	AK, ZD	AK	AK, HZ
Resources	RW	AA, RW, OT	RW, EBF, EGF	RW, XH
Supervision	RW	RW	RW, EGF	RW, ZH
Visualization	AK	AK	AK	AK
Writing (original draft)	AK	AK	AK	AK
Writing (review and editing)	AK, YL, RW	AK, ZD, AA, OT, RW	AK, HZ, EBF, EGF, RW	AK, HZ, LL, XH, RW

Other publications not included in this thesis

Zhang, H., Kizyte, A., & Wang, R. (2024). Enhancing dynamic ankle joint torque estimation through combined data augmentation techniques. *2024 10th IEEE RAS/EMBS International Conference for Biomedical Robotics and Biomechatronics (BioRob)*, 198–203. doi: 10.1109/BioRob60516.2024.10719753

Corell, L., Hjalmarsson, E., Fernandez-Gonzalo, R., Edman, S., Kizyte, A., Wang, R., Kruse, A., Pontén, E., Norrbom, J., & Von Walden, F. (2024). Disproportional ventilatory response to acute incremental exercise in individuals with cerebral palsy. *Gait & Posture, 113*, 240–241. doi: 10.1016/j.gaitpost.2024.07.257.

List of abbreviations

ASIA	American Spinal Injury Association
CCI	Co-contraction index
CIS	Common input strength
CKC	Convolutional kernel compensation
CMC	Corticomuscular coherence
CNN	Convolutional neural network
CoV	Coefficient of variation
CST	Cumulative spike train
EEG	Electroencephalography
EMG	Electromyography
FAC	Functional ambulation category
FMA	Fugl-Meyer Assessment
HDEMG	High-density EMG
ISI	Inter-spike interval
IP	Inert period
LIF	Leaky integrate-and-fire
MAS	Modified Ashworth scale

ML	Machine learning
MMT	Manual muscle testing
MN	Motor neuron
MU	Motor unit
MVC	Maximal voluntary contraction
NRMSE	Normalized root mean squared error
NMS	Neuromusculoskeletal
PC	Principal component
PCA	Principal component analysis
PNR	Pulse-to-noise ratio
RNN	Recurrent neural network
SCI	Spinal cord injury
SOL	Soleus
SVR	Support vector regression
TA	Tibialis anterior

CONTENTS

1 Introduction

The control of human movement relies on the seamless integration of neural drive and musculoskeletal dynamics. Neurological conditions such as spinal cord injury (SCI) and stroke disrupt this integration, leading to neuromuscular impairments that compromise voluntary force production and, therefore, movement. These impairments not only affect individual quality of life but also pose significant public health challenges. In Sweden, the incidence rates of stroke have been steadily decreasing over the years, however in 2023 there were still approximately 325 strokes occurring per 100,000 inhabitants [1], while the incidence of SCI ranged between 23.0 and 25.4 per million inhabitants each year from 2016 to 2020 [2]. The societal importance of tackling these challenges is also reflected in their alignment with the United Nations Sustainable Development Goal 3, which strives to ensure healthy lives and promote well-being for all individuals across their lifespan. Rehabilitation plays a crucial role in improving the quality of life for individuals living with SCI and stroke, helping their recovery of motor function, independence, and participation in daily activities.

Accurate joint torque estimation is important for the effective control of robotic rehabilitation devices, such as exoskeletons. These devices aim to provide assistive torque that aligns with the user's intended movements, enhancing the efficacy of rehabilitation training. For instance, integrating electromyographic (EMG) signals into control algorithms allows exoskeletons to adaptively assist users based on their muscular effort, thereby promoting active participation during therapy sessions [3-5]. Moreover, computational modeling approaches, such as EMG-driven neuromusculoskeletal (NMS) models, facilitate torque estimation while simultaneously allowing identification of neuromuscular

parameters, offering valuable insights into the underlying mechanisms of motor control [6, 7]. However, changes in these parameters due to neurological pathologies are not always fully understood, highlighting the importance of fundamental observational studies. Such studies can shed light on neural adaptations in individuals with disabilities, potentially serving as biomarkers to inform and optimize rehabilitation interventions.

High-density electromyography (HDEMG) provides a non-invasive, spatially detailed means of investigating muscle activation and motor unit (MU) behavior. By capturing surface EMG signals from dense electrode grids, HDEMG enables the signal decomposition into individual MU spike trains and the extraction of spatial and neurophysiological features related to the underlying neural drive [8, 9]. This has important implications for both torque estimation and the assessment of neuromuscular impairments at the MU level. When paired with computational modeling and advanced signal processing, HDEMG offers new possibilities to study how neuromuscular impairments influence motor control strategies in vivo.

This thesis aims to explore how HDEMG can enhance ankle joint torque estimation by incorporating neurophysiological data and spatial distribution of muscle activation and advance our understanding of ankle neuromechanics in individuals with SCI and stroke. These aims are addressed across four studies using a combination of HDEMG, EEG, machine learning, signal processing, and computational neuromusculoskeletal modeling.

Studies I and II focus on torque estimation. Study I evaluates how machine learning (ML) techniques, including support vector regression (SVR) and deep learning models, predict isometric ankle torque from bipolar EMG, HDEMG, and extracted spatial and neurophysiological features. The findings show that although ML models perform well under static conditions, their accuracy decreases in dynamic tasks, emphasizing the need for physiologically informed constraints in torque prediction. Moreover, ML models offer no physiological insight into the underlying neuromuscular mechanisms. Addressing this, **Study II** incorporates a cumulative spike train (CST)-driven motoneuron pool model into a neuromusculoskeletal modeling framework. By using decomposed MU spike trains to simulate neural drive and muscle force production, this study provides a more neurophysiologically interpretable representation of joint torque generation.

Studies III and IV investigate MU-level alterations following motor impairment. **Study III** uses HDEMG decomposition to characterize changes in

MU firing behavior and spectral properties in individuals with SCI. The findings reveal altered MU recruitment and compensatory motor strategies, contributing to our understanding of how the neuromuscular system adapts after injury. **Study IV** introduces a novel MU-based corticomuscular coherence (CMC) analysis in individuals with stroke, examining the shared synaptic input between groups of MUs and the motor cortex. The results suggest that MU-level CMC is shaped by networks of neurons rather than individual MU properties and reveal increased CMC spatial entropy on the paretic side, indicating cortical reorganization and altered corticospinal connectivity.

Collectively, this thesis demonstrates how integrating HDEMG, computational modeling, and neurophysiological analysis can enhance both torque estimation and the assessment of pathological motor control. These advances hold implications for rehabilitation, assistive device development, and physiologically informed modeling approaches in neuromechanics.

2 Background

This chapter presents theoretical foundations pertinent to this thesis, including the biomechanics and physiology of ankle joint torque generation, methods for interfacing neural control pathways, and signal processing techniques for EMG, EEG, and coherence analysis. It further outlines approaches for modeling the motor neuron (MN) pool and estimating joint torque using neuromusculoskeletal models and machine learning. Lastly, it describes neuromuscular disorders such as spinal cord injury and stroke, along with their clinical evaluation.

2.1 Biomechanics and physiology of ankle joint torque generation

2.1.1 Relevant anatomy of the ankle joint

The ankle joint comprises three primary articulations: the talocrural, subtalar, and midtarsal (calcaneocuboid and talonavicular) joints. Together, these structures facilitate movement across three anatomical planes (Figure 2.1 a). Among the articulations, the talocrural joint – a uniaxial hinge joint formed by the tibia, fibula, and talus – has the largest range of motion. This joint enables sagittal plane movements: dorsiflexion (tilting the foot upward) and plantarflexion (tilting the foot downward). Dorsiflexion is primarily driven by the tibialis anterior (TA), whereas plantarflexion is mainly controlled by soleus (SOL), gastrocnemius, and tibialis posterior. The subtalar joint, located between the talus and calcaneus, allows movement in the frontal plane, while the

midtarsal joint, comprising the calcaneocuboid and talonavicular articulations, enables the transverse plane motion [10]. However, during most daily activities, these movements do not occur in isolation but rather as coordinated motions across multiple planes. Notably, two key tri-planar movements – pronation and supination—integrate motion from all three planes, contributing to dynamic stability during locomotion.

This thesis focuses on muscles responsible for controlling ankle movements in the sagittal plane as they generate the highest torques over the greatest range of motion compared to movements in other planes. Particularly, the emphasis is on the TA muscle; however, the activity of its antagonists, including SOL (Studies I-III), peroneus longus (Study I) and gastrocnemius (Studies I-II), is also assessed. These muscles play a crucial role in fundamental locomotor functions such as walking, running, stair climbing, and maintaining balance.

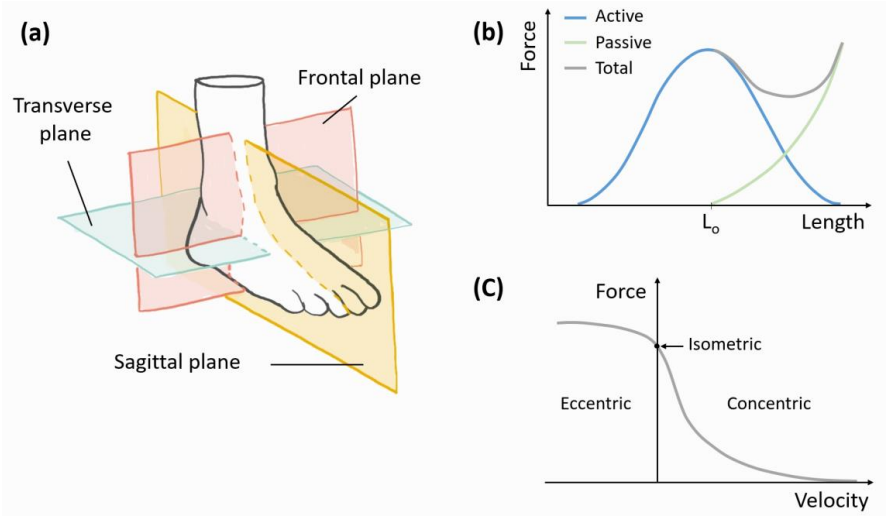

Figure 2.1 (a) Anatomical planes of the foot and ankle. (b) A schematic illustration of the force-length relationship, showing the muscle force production capacity as the sum of active and passive components. Maximum force is generated at the optimal muscle length (Lo). (c) A schematic representation of the muscle force-velocity relationship across different contraction types: eccentric (lengthening), isometric (constant length), and concentric (shortening) [11].

2.1.2 Architecture of a skeletal muscle

Skeletal muscle consists of bundles of muscle fibers, each containing numerous myofibrils. Each myofibril is made up of repeating units called sarcomeres, which serve as the fundamental contractile units of muscle. Within each

sarcomere, actin and myosin filaments are arranged in an overlapping pattern, allowing force generation through cross-bridge cycling (Figure 2.2). The hierarchical organization of skeletal muscles, from individual sarcomeres to entire muscles, enables efficient force production and movement. Muscle architecture, i.e. the organization and phenotype of muscle fibers, as well as the composition of other intramuscular tissues plays a significantly role in determining muscle function.

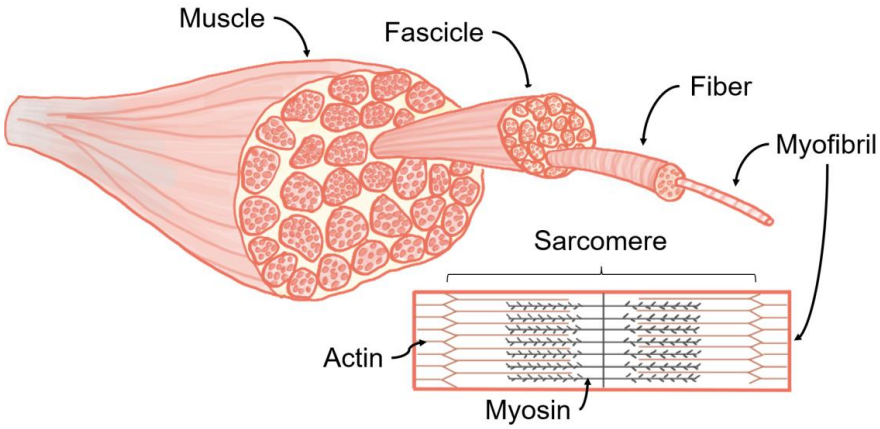

Figure 2.2 The hierarchical structure of the muscle.

Skeletal muscle fibers are classified by contraction speed and fatigue resistance into slow-twitch (Type I) and fast-twitch (Type IIa and IIx) fibers, with Type I being fatigue-resistant and Type IIx generating high force but fatiguing rapidly. The proportion of these fibers varies by muscle, influencing their functional roles. For example, the soleus, rich in Type I fibers, is suited for sustained, weight-bearing activities. Muscle architecture also affects force production: parallel muscles favor faster movement due to greater shortening capacity, while penniform muscles, with obliquely arranged fibers, generate higher force at reduced contraction velocity. The pennation angle, which increases during contraction, modulates the proportion of fiber force transmitted to the tendon. Although muscle volume often correlates with strength, factors such as fiber type composition, architecture, and neural activation critically determine force capacity. Muscle composition and function are dynamic, influenced by genetics, aging, activity, and pathology, all of which alter the balance between contractile and non-contractile tissue and impact neuromechanical performance.

2.1.3 Biomechanics of joint torque generation

From an engineering perspective, net torque τ (eq. 1) generated at a joint at a certain time instance results from the collective action of multiple agonist and antagonist muscles, each producing a force F at a specific moment arm r, which depends on the muscle's anatomical attachment points and joint configuration:

$$\boldsymbol{\tau}_{joint} = \sum_{i} \boldsymbol{r}_i \times \boldsymbol{F}_i \quad (1)$$

Muscle force production is governed by both neural activation and muscle architecture, while moment arms are shaped by joint geometry, muscle path and vary with joint angle. Because muscle length changes with joint position, the overlap between actin and myosin filaments also varies, directly affecting the number of cross-bridge formations. As a result, muscle force production is inherently non-linear and can be described using the force-length relationship (Figure 2.1 b) [12]. Additionally, active muscle force depends on contraction velocity and contraction type (Figure 2.1 c): isometric (static), eccentric (lengthening), or concentric (shortening) [13].

Biarticular muscles, which span two joints, introduce additional complexity by distributing force across both joints based on their relative positions. For instance, the gastrocnemius, which crosses both the knee and ankle, function as a more powerful plantar flexor when the knee is extended compared to when it is flexed [10]. This behavior arises due to changes in muscle length and moment arm, which influence force production and mechanical advantage.

2.1.4 Physiology of volitional muscle control

Volitional motor control originates in the cortical regions of the brain, where motor commands are generated in areas such as the primary motor cortex. These commands are transmitted via upper MNs through descending pathways, most notably the corticospinal tract, which plays a critical role in voluntary movement. The corticospinal tract decussates (crosses over) at the medulla before continuing down to the spinal cord, synapsing with alpha (lower) MNs (Figure 2.3 a). In addition to descending pathways, ascending pathways such as the spinothalamic tract and dorsal columns carry sensory information from the muscles back to the brain, providing essential feedback for the regulation and refinement of motor commands. While cortical structures are responsible for higher-level functions, including movement planning and coordination, the spinal cord handles lower-level control, including the spatiotemporal coordination of individual muscles and the gradation of force output [14].

Within the spinal cord, motor control involves both rapid, direct monosynaptic pathways (e.g. stretch reflex) as well as more complex polysynaptic circuits involving interneurons, with additional polysynaptic pathways connecting to supraspinal centers for higher-level motor regulation.

Each skeletal muscle is innervated by a MN pool – a cluster of MNs located in the ventral horn of the spinal cord. The MNs within this pool innervate a number of muscle fibers in the muscle, forming a MU – the fundamental functional unit of the neuromuscular system [15]. A single muscle typically comprises many MUs of varying sizes. When a MN generates an action potential, the signal propagates along its axon and reaches the muscle fibers it innervates, inducing their simultaneous depolarization and generating a MU action potential. The MU action potentials trigger muscle fiber contractions and generate muscle force. However, coordinated recruitment and activation of multiple MUs is needed to generate desired muscle contractions.

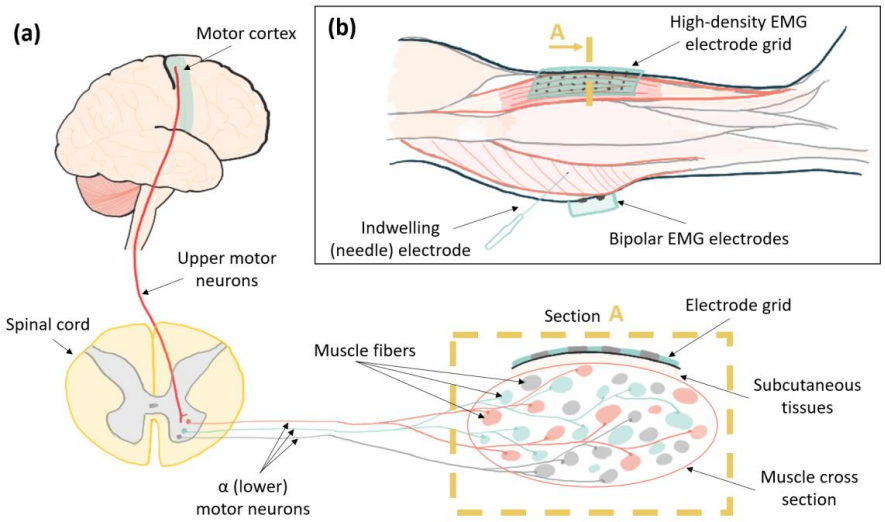

Figure 2.3 Schematic representations of a descending motor control pathway (a) and EMG measurement methods (b) [11].

Force modulation within a muscle is governed by two key mechanisms: MU recruitment and rate coding. At lower forces, the modulation is primarily through MU recruitment, while at higher forces, rate coding plays a more significant role [16]. MU recruitment refers to the number of MUs activated and their systematic recruitment based on the size during muscle contraction. To generate greater force, more MUs are recruited in an orderly fashion, from the

smallest to the largest, in accordance with Henneman's size principle [17, 18]. Rate coding refers to the increase in the discharge rate of MUs (the frequency at which MNs send pulses to the muscle fibers), which also contributes to increased muscle force [19].

2.2 Interfacing neural control pathways

Measuring neural control signals is essential for understanding how the brain coordinates and controls movement, providing insights into motor function, motor learning, and rehabilitation. Due to limited access to the upper MNs within the spinal cord, these signals are typically measured at either the cortical or muscle level. The most common *in vivo* measurement techniques include electroencephalography (EEG) and EMG. EEG captures electrical activity at the cortical level, revealing information about movement initiation, planning, and high-order motor control. EMG records the electrical signals propagating along muscle fibers, allowing for the assessment of muscle activation during movement.

2.2.1 EEG

EEG is a non-invasive technique that measures the electrical activity of the brain by placing electrodes on the scalp. It is widely used to assess motor-related brain activity, particularly in regions involved in movement planning, initiation, and control, such as the motor cortex, premotor cortex, and supplementary motor area. EEG allows real-time observation of cortical activity, capturing characteristic neural rhythms such as beta waves, which are strongly associated with motor processes [20-22]. By recording the brain's electrical signals during movement tasks, EEG offers valuable information into the neural mechanisms underlying motor control. Given its high temporal resolution, EEG is ideal for studying the dynamic aspect of motor-related brain activity [23].

2.2.2 EMG

EMG is a technique used to record the electrical activity produced by muscles during contraction. MU action potentials propagate through the tissues to the skin's surface, where their combined activity can be detected by EMG electrodes [14]. However, due to the variations in MU depths within the muscle and differences in the number of muscle fibers innervated by each MN, not all MUs contribute equally to the recorded EMG signal. As a result, it is crucial to distinguish between neural drive – the total number of MU action potentials

generated within the muscle – and muscle activation – the subset of muscle fiber action potentials that are detectable by the EMG electrodes [15].

There are two primary methods for EMG recording: indwelling EMG and surface EMG (Figure 2.3 b). Indwelling EMG involves inserting needle electrodes into the muscle, providing precise measurements of MU activity due to the proximity of the electrodes to individual MUs. However, it is invasive, potentially causing discomfort and carrying a risk of infection. In contrast, surface EMG uses electrodes placed on the skin above the target muscle (non-invasive). While surface EMG offers a global representation of the MU activity and is more comfortable for long-term use, it has limitations in isolating individual MUs due to the distance from the MUs and potential signal interference from surrounding tissues. Surface EMG can be performed with either bipolar electrodes or high-density (HDEMG) grids comprising multiple electrodes. HDEMG enables *in vivo* observation of MUs by leveraging advanced signal processing techniques while preserving the advantages of surface EMG.

In this thesis, we primarily focus on HDEMG, as it has been shown to enhance muscle force estimation [24] and offers a non-invasive approach to studying MU activity.

2.3 Signal processing

Signal processing plays a crucial role in both observational studies and computational modeling of neuromuscular and neurophysiological function. In observational studies, advanced signal processing techniques applied to EEG and EMG signals enable the extraction of meaningful neural and muscular activity patterns, helping to identify biomarkers for motor control and neurological disorders [25]. In computational modeling, precise EMG processing is essential for estimating accurate neural drive, which serves as inputs for NMS models to simulate muscle activation and movement.

In this chapter, we will discuss signal processing techniques relevant to this thesis.

2.3.1 EMG processing

The EMG signal $e(t)$ represents a composite recording of multiple MU action potentials $h_i(t)$ (eq. 2), which are influenced by the filtering effects of interposing tissues:

$$e(t) = \sum_{i=1}^{N} \sum_{j} s_i(t - t_{ij}) * h_i(t) \quad (2)$$

where N is the number of active MUs, $s_i(t)$ is the spike train of the i-th MU, modeled as a series of delta functions with t_{ij} being the firing time of the j-th action potential (spike) from the i-th MU.

Surface EMG recordings are often affected by various sources of noise, including crosstalk from adjacent muscles, physiological artifacts such as cardiac signals, motion artifacts, and electrical interference from the environment. Additionally, raw EMG signals are inherently complex and challenging to interpret without proper processing. To enhance signal quality and improve interpretability, EMG signal is typically processed through filtering and feature extraction. These processing techniques can generally be categorized into time domain and frequency domain methods.

Time-domain processing focuses on analyzing the raw EMG signal amplitude and temporal characteristics to extract meaningful features related to muscle activation. Common preprocessing steps include bandpass filtering (e.g., 10–450 Hz) to remove motion artifacts, DC offset, and high-frequency electrical noise while preserving relevant neural signal. The choice of cutoff frequencies is based on the spectral content of the EMG signal, as frequencies below 5 Hz often contain movement artifacts, whereas frequencies above 500 Hz may include electromagnetic interference with no meaningful EMG spectral components [26]. Following filtering, rectification (taking the absolute value of the signal) is commonly applied to ensure all values are positive, allowing for better representation of muscle excitation. To further enhance interpretability, the EMG envelope is extracted by applying a low-pass filter (typically 2–10 Hz) to smooth the rectified signal, highlighting the slow shifts in muscle excitation that best correlates with muscle activation. Although the EMG envelope is one of the most used representations, other time-domain features, such as the moving root mean square (RMS), are frequently used in biomechanical modeling and real-time neuromuscular control applications [27]. These features offer information on muscle excitation and indirectly reflect MU recruitment patterns.

Frequency-domain analysis transforms the EMG signal into its spectral components, providing insights into neuromuscular control, muscle fatigue, and MU behavior. The most common approach is the fast Fourier transform [28], which decomposes the signal into its frequency components, allowing for the examination of power spectrum distribution. However, Fourier transform-

based methods assume signal stationarity, a condition may not always hold for EMG signals, especially during dynamic tasks. To address this limitation, an alternative and widely used method is Welch's power spectral density estimation [29]. This technique improves spectral accuracy by segmenting the EMG signal into overlapping windows, applying a window function to each segment, and averaging the resulting periodograms. This approach reduces variance in the spectral estimate while preserving frequency resolution.

2.3.1.1 HDEMG processing

EMG parameters alone are not directly reflective of MU behavior. To estimate the neural drive to muscle, it is essential to decompose the EMG recordings into the contributions of individual MUs [15]. Historically, the decomposition of MU activity began with template matching algorithms, which detect MU action potentials by comparing their waveform shape to predefined templates. While these early methods remain used today for intramuscular EMG, they were initially limited in their ability to distinguish action potentials from different MUs that overlapped in time [30] [31]. Over time, the field has advanced with techniques such as blind source separation. Unlike template matching, these data-driven methods separate source signals from a set of mixed observations without requiring predefined templates, improving the accuracy of MU decomposition, especially in surface EMG [32]. However blind source separation algorithms operate on the assumption that the number of observations (i.e. electrodes) exceeds the number of sources (i.e. MUs). Consequently, these algorithms can only be applied to HDEMG signals, and not bipolar EMG.

One of the most prominent blind source separation techniques is convolutional kernel compensation (CKC), which has been widely used for HD-EMG decomposition [33] [32]. The CKC method models the recorded signal, $x(n)$, at the n-th sample as a linear mixture of source signals and their time-delayed representations, with additive white noise $\omega(n)$:

$$\boldsymbol{x}(n) = \boldsymbol{H}\boldsymbol{t}(n) + \boldsymbol{\omega}(n) \tag{3}$$

where H is the mixing matrix of all channel responses (convolution kernels), and $t(n)$ is the vector of input signals from all sources. The CKC algorithm estimates the MU spike train $\hat{t}_j(n)$ for each MU by using cross-correlation matrices (eq. 4) and iterative gradient descent optimization (eq. 5) to refine the decomposition. The MU spike train for the j-th MU, $\hat{t}_j(n)$, is estimated as:

$$\hat{t}_j(n) = \boldsymbol{c}_{t_j x}^{\ T} \boldsymbol{C}_{xx}^{-1} \boldsymbol{x}(n) \tag{4}$$

where C_{xx} is the cross-correlation matrix of the recorded signals $x(n)$, and c_j is an unknown cross-correlation vector of x and $t_j(n)$, which can be iteratively estimated using gradient descent. The gradient descent update rule for the cross-correlation vector is given by:

$$\boldsymbol{c}_{\hat{t}_j x} = \boldsymbol{c}_{\hat{t}_j x} - \eta(k) \boldsymbol{F}\left(\hat{t}_j\right) \tag{5}$$

where $F\left(\hat{t}_j\right)$ is the cost function calculated as the sum of the gradient of the source signal with respect to the MU spike train, and $\eta(k)$ is the learning rate at the k-th iteration [32]. The CKC method has been validated for isometric contractions and has proven useful in studies of pathologies like tremor [34], stroke [35], and spinal cord injury [36]. Although the method can automatically detect MU firing events, manual editing is still necessary to ensure the quality of the decomposition, which can be assessed through metrics like pulse-to-noise ratio (PNR) [33] and silhouette score [37]. Despite recent improvements, the HDEMG decomposition is still an active field of research, especially for applications involving dynamic movements [9, 38, 39], as the CKC method currently works best in isometric conditions.

Once the MU spike trains are reliably identified, various MU parameters can be extracted, such as the variation in inter-spike intervals (ISI), MU discharge rates, and recruitment/de-recruitment thresholds. The ISI, which represents the time between adjacent spikes, is typically regular but may show irregularities in pathological conditions such as Parkinson's disease [40]. The MU discharge rate which quantifies the frequently at which MU fires, is directly correlated to the force production. While an increase in discharge rate is needed for greater muscle activation, it is also limited by factors such as muscle composition and pathological conditions. The recruitment and de-recruitment thresholds correspond to the torque levels at which MUs begin and stop firing continuously. These thresholds can change due to factors like fatigue or neuromuscular impairments [41]. Together with discharge rates, the recruitment thresholds provide valuable insight into force modulation strategies within the muscle, contributing to a deeper understanding of muscle performance and neuromuscular control [42].

2.3.2 EEG processing

EEG signals are often contaminated by various noise sources, including power line interference, movement artifacts, eye blinks, and muscle activity. Proper

preprocessing and feature extraction are crucial for improving signal quality and enabling meaningful analysis.

EEG preprocessing typically begins with bandpass filtering, commonly in the range of 0.5–100 Hz, to remove slow drifts and high-frequency noise while preserving physiologically relevant oscillations. A notch filter at 50/60 Hz is often applied to eliminate power line interference. Common artifact removal techniques include independent component analysis, which separates sources of noise from neural signals by decomposing EEG into statistically independent components; regression-based methods, which subtract known artifacts such as electrooculographic or EMG contamination; and adaptive filtering, which dynamically adjusts filter parameters to suppress noise while preserving neural activity [43].

Similarly to EMG, EEG analysis can be performed in both the time and frequency domains, depending on the research question. Time domain analysis focuses on measures such as event-related potentials to capture transient brain responses to stimuli, typically averaged over multiple trials to improve signal-to-noise ratio [23]. While frequency domain analysis uses power spectral density estimation to study the distribution of EEG power across frequency bands (δ: 0.5 – 4 Hz, θ: 4 – 8 Hz, α: 8 – 15 Hz, β: 15 – 30 Hz, γ: 30 -100 Hz) [23].

In this thesis we focus solely on the frequency domain analysis of the EEG signals with particular emphasis on the β frequency band, which is specifically associated with isometric muscle contractions [20-22].

2.3.3 Coherence analysis

Coherence analysis serves as a powerful tool for quantifying the frequency-domain synchronization between two signals, offering means to explore their functional connectivity and shared neural information. A general definition of coherence C at frequency f is given by equation 6:

$$C_{xy}(f) = \frac{|S_{xy}(f)|^2}{S_{xx}(f) \cdot S_{yy}(f)} \tag{6}$$

Where S_{xy} is the cross-power spectral density between signals x and y, S_{xx} and S_{yy} are the power spectral densities of signals x and y respectively [44].

Corticomuscular coherence (CMC) between EEG and EMG assesses the strength of coupling between cortical activity and muscle activation, providing insights into sensorimotor integration and motor control [45]. In addition, intra-

muscular coherence, which examines frequency-domain correlations between EMG signals recorded from different locations or between decomposed MU cumulative spike trains (CSTs) within the same muscle, can reveal synchronized MU behavior and common synaptic input to MNs [46]. These coherence methods are particularly useful in studying neuromuscular disorders and motor adaptation, as altered coherence patterns often indicate changes in MU synchronization and neural drive [47-49].

2.4 Modeling the motor neuron pool

Since MU decomposition cannot capture the activity of all MUs within a muscle, MN modeling remains the primary approach for expanding the recorded MU pool, enabling the study of neuromuscular control at a level of the entire MU pool. Individual MNs form the common pathway of the nervous system; however, muscle contraction and consequently movement is driven by the coordinated activity of an entire MU pool — a population of MNs innervating fibers of a muscle. By modeling the entire MU pool, we can capture recruitment dynamics, discharge modulation, and force generation, offering a more complete picture on both intact and pathological motor control. Computational models used to simulate MN behavior enable the study of neural firing patterns and responses to synaptic input.

One of the most widely used MN models is the Hodgkin-Huxley (HH) model [50], which describes neuronal membrane potential dynamics by modeling the behavior of ion channels. The HH model is defined by a set of differential equations representing the flow of sodium, potassium, and leak currents across the neuronal membrane. Although it offers high biofidelity, the HH model is computationally demanding. A more computationally efficient alternative is the Leaky Integrate-and-Fire (LIF) model [51]. The LIF model retains key features of neuronal spiking while significantly reducing computational cost, making it suitable for studying MN recruitment and synchronization [52]. LIF model approximates neuronal spiking behavior as a simplified system where the membrane potential V_m gradually integrates incoming synaptic inputs over time (eq. 7) until it reaches a predefined threshold V_{th} (eq. 8), at which point a spike is generated, and the membrane potential is reset to V_{reset}:

$$C_m \frac{dV_m}{dt} = -g_l(V_m - V_L) + I \tag{7}$$

with the threshold condition:

$$V_m(t) \geq V_{th} \quad \Rightarrow \quad V_m(t+\Delta) = V_{reset} \tag{8}$$

Where C_m is the membrane capacitance, I is the input current, g_l is the leak conductance, V_L is the leak reversal potential, Δ represents the reset interval.

The transition from single MN modeling to estimating the behavior of the entire MU pool requires accurate MN parameter identification. While certain properties such as recruitment thresholds and discharge rates can be directly extracted from decomposed MUs, other characteristics like MN size and synaptic input properties must be estimated computationally. Due to its high biofidelity, the Hodgkin-Huxley model enables estimation of parameters like soma size, potassium channel dynamics and synaptic conductance [53, 54]. LIF-based MN pool models, while less physiologically accurate, have also been increasingly used for in vivo MU parameter estimation. These computational models can efficiently approximate MN pool recruitment dynamics by capturing parameters such as MN surface area, reset times, and synaptic input properties [55].

Optimizing MN models to match experimental data requires advanced parameter fitting techniques. Common approaches include genetic algorithms [53] and particle swarm optimization [56], which iteratively refine model parameters to improve physiological accuracy.Alternatively, firing rate matching has been employed to ensure that the recruitment and discharge behaviors of the model reflect those observed experimentally [55].

While these techniques are often applied to single MN models, scaling up to a full MU pool involves modeling the collective behavior of many interconnected MNs, each with varying properties such as size, recruitment threshold, and excitability. This enables the simulation of population-level dynamics that more closely represent the distributed control of muscle force. Scaling MN modeling from single neurons to the full MU pool enables deeper insights into neuromuscular function, force generation, and the mechanism underlying motor impairments. This approach is particularly valuable for investigating neurological disorders, where altered MU pool dynamics can reveal pathological changes in motor control and may inform the understanding of compensatory or recovery mechanisms.

2.5 Methods for torque estimation

Torque estimation methods generally fall into two main categories: NMS models and machine learning (ML) approaches. NMS models rely on biomechanical

and physiological principles, integrating muscle activation (e.g., from EMG) with musculoskeletal dynamics to estimate joint torque. These models offer high interpretability and can provide physiologically meaningful insights but often require precise subject-specific calibration and are sensitive to modeling assumptions [57-59]. In contrast, ML approaches use data-driven techniques to learn direct mappings between input signals (e.g., EMG and joint kinematics) and torque output. These methods can often efficiently capture complex, nonlinear relationships and achieve high accuracy without explicit physiological modeling [60, 61]. While ML methods can handle complex, nonlinear relationships efficiently, they provide limited physiological interpretability, require large training datasets, and may lack generalizability beyond training conditions. The choice between these two approaches ultimately depends on the intended application, with NMS models preferred for mechanistic understanding, and ML models better suited for real-time torque prediction.

2.5.1 Neuromusculoskeletal models

NMS models provide a physiologically grounded framework to estimating joint torque by integrating neural drive, muscle activation dynamics, and musculoskeletal mechanics (Figure 2.4). Among various NMS models proposed in the literature, this thesis focuses on the OpenSim [62] and CEINMS [7] implementations, which are among the most widely used approaches. In a forward NMS model, neural drive serves as the model input, while muscle forces or joint torques are the outputs. The core modeling process involves transforming neural excitation into muscle activation, which is then translated into muscle force through contraction dynamics. Finally, joint torque is computed based on musculoskeletal model geometry.

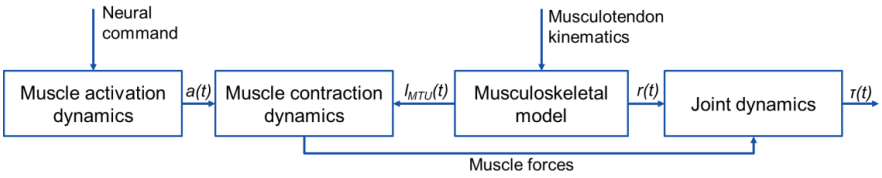

Figure 2.4 Schematic structure of the open-loop forward neuromusculoskeletal model. Here a(t) represents muscle activations, $l_{MTU}(t)$ – musculotendon lengths, r(t) – moment arms defined by the muscle attachments, τ(t) – joint torques.

The relationship between neural drive $e(t)$ and neural activation $u(t)$ can be modeled as a piecewise parametric function [63], a differential system with time

delays, or a continuous-time dynamic system. In this thesis, it is modeled as a critically dampened linear second-order differential system (eq. 9) [64, 65]:

$$u(t) = \alpha \cdot e(t-\tau) - \beta_1 \cdot u(t-1) - \beta_2 \cdot u(t-2), \quad (9)$$
$$\beta_1 = C_1 + C_2,$$
$$\beta_2 = C_1 \cdot C_2,$$
$$\alpha - \beta_1 - \beta_2 = 1$$

where α is the muscle gain parameter, β_1 and β_2 are recursive parameters ensuring stability, and τ represents the electromechanical delay. The neural activation $u(t)$ is then transformed into muscle activation $a(t)$ using non-linear relationship [64] described by equation 10:

$$a(t) = \frac{e^{A \cdot u(t)} - 1}{e^{A} - 1} \quad (10)$$

where A is a shape factor that defines the activation curve. Once the muscle activation is obtained, contraction dynamics are typically modeled using a Hill-type muscle model (eq. 11) to estimate muscle forces [66], which estimates force based on active (muscle) and passive (tendon) force contributions:

$$F = F_0^m \left[F_a(l) \cdot F_v(v) \cdot a + F_p(l) + d_p \cdot v \right] \cdot \cos(\theta) \quad (11)$$

where F_0^m is the maximum isometric force, $F_a(l)$ and $F_v(v)$ represent the force-length and force-velocity relationships, respectively, $F_p(l)$ accounts for passive force contributions, d_p is the muscle damping parameter, v is the contraction velocity, and θ is the fiber pennation angle. The joint torque τ_j is then computed by summing the contributions of all m muscles acting across a joint, each weighted by its respective moment arm r_m (eq. 1).

2.5.1.1 Estimating neural drive

Estimating neural excitation is a critical, yet often oversimplified step in NMS modeling, as it serves as the link between neural control and musculoskeletal function. Neural excitation represents the central nervous system's output to muscles and dictates the timing and intensity of muscle contractions. Inaccurate representation of neural drive can lead to misrepresentation of motor control strategies, leading to errors in torque estimation and limit the model's applicability in personalized simulation and assistive device control. There are several approaches to estimating neural excitation in NMS models, each with different trade-offs in terms of physiological fidelity, computational cost, and real-time feasibility. The primary methods include EMG-driven models, MU spike train-driven models.

EMG-driven models estimate neural excitation using the processed EMG envelope, which is assumed to reflect the overall neural drive to the muscle. The raw EMG signal is typically rectified and low-pass filtered to obtain a smooth representation of muscle activation patterns. This method is computationally efficient, relatively simple to implement, and suitable for real-time applications such as rehabilitation and assistive device control [67, 68]. However, it does not capture individual MU behavior, and thus fails to represent important neuromuscular control mechanisms, such as MU recruitment and discharge rate modulation. Despite these limitations, EMG-driven models are widely used in biomechanics due to their practicality and ease of implementation.

In contrast, MU spike train-driven models derive neural excitation by decomposing the EMG signal into individual MU action potentials. This allows for a detailed representation of MU recruitment and firing patterns, providing deeper understanding of neuromuscular control strategies [69, 70]. By considering individual MU activity, these models can capture subtle changes in neural control, such as adaptations in recruitment thresholds and modulation of discharge rates under different loading conditions. However, accurate MU decomposition remains a technical challenge, requiring complex algorithms and high-quality HDEMG recordings [71]. Despite these challenges, MU spike train-driven models are valuable for advancing fundamental research in motor control and neuromuscular physiology.

An extension of MU spike train-driven models involves estimating neural excitation from the entire MU pool rather than relying solely on decomposed spike trains. As discussed in section 2.3.1.1, in-vivo observation of the full MU pool is not currently feasible. To address this limitation, in silico models are being developed to extrapolate from a measured subset of MUs to estimate the activity of the entire MU pool [55]. These MU pool-driven models aim to reconstruct cumulative MU activity by incorporating computational frameworks that account for the distribution of MU recruitment thresholds and discharge properties across the MU pool. One such approach represents each MU as an individual force generator unit and aggregates their contributions across the whole MU population, providing a population-level estimate of neural drive [72]. This method allows for a balance between physiological detail and computational feasibility, while it does not require full MU decomposition but still incorporates critical information about recruitment and rate coding. However, similar to MU spike train-driven models, this approach depends on

accurate characterization of MU behavior and may be sensitive to quality of HD-EMG decomposition.

2.5.2 Machine learning

The relationship between EMG amplitude and muscle force is well established with EMG signals generally increasing as force production rises [73]. This relationship extends to joint torque, however, it is non-linear and influenced by factors such as movement type and muscle contraction dynamics. Owing to this relationship, features derived from the EMG envelope or amplitude are commonly used as input features in ML models for torque or force prediction [74], [75, 76]. The EMG envelope is typically extracted by rectification and low-pass filtering, though comparable results can be obtained by computing statistical or frequency-based features within a moving window, which also helps reduce the number of samples — potentially beneficial in real-time applications.

A variety of ML models have been applied to torque and force estimation. Artificial neural networks such as multi-layer perceptron [74], recurrent neural networks (RNNs) [60], and convolutional neural networks (CNNs) [75] [77] have demonstrated promising performance due to their ability to capture complex relationships in time and space. However, these models often require large amounts of training data to generalize across different individuals and movements. Collecting high-quality EMG data can be time-consuming, leading to small sample sizes that increase the risk of overfitting — a phenomenon where the model learns to replicate training data but fails to generalize to unseen data. Alternatively, support vector regression (SVR) provides a more data-efficient approach, achieving comparable torque estimation performance to simple neural networks while requiring less training data [78] [79]. However, SVR requires manual feature extraction, which can be labor-intensive.

A potential solution to manual feature extraction is using CNNs as feature extractors, followed by a regression algorithm for torque prediction. CNNs can automatically learn spatial features from HDEMG electrode grids. Furthermore, CNNs can be combined with RNN architectures (e.g., CNN-RNN models) to capture that capture both spatial and temporal dependencies, leading to improved prediction accuracy in dynamic tasks [80]. Alternatively, dimensionality reduction techniques like principal component analysis (PCA) are often used to remove redundancy from highly correlated EMG data and extract the salient features. The choice of method depends on the application

requirements — deep learning models offer automatic feature extraction and the ability to model complex non-linear relationships, while SVR and PCA-based approaches are more suitable for smaller datasets and computationally constrained environments.

2.5.2.1 Principal component analysis

PCA is a widely used statistical technique for reducing data dimensionality while preserving as much variance as possible. In machine learning applications, it is often employed as a preprocessing step to simplify data representation and improve computational efficiency. In EMG research, PCA has been previously applied to HDEMG for dimensionality reduction [81], helping to extract dominant motor control patterns while minimizing redundancy across highly correlated electrode channels [24, 82].

PCA is an unsupervised learning method that identifies vectors, known as principal components (PCs), along which the data exhibits the most variance. The first principal component (PC1) captures the maximum variance, while subsequent components are ranked in decreasing order of explained variance [83]. Each PC is a linear combination of the original data features, meaning that the data is transformed into a new coordinate system where the axes correspond to these components. Mathematically, if X represents the original n × p data matrix with n samples and p features, PCA finds a projection matrix Q such that $F = XQ$, where F is the transformed data matrix with the same number of samples but fewer features. The columns of Q are the eigenvectors of the covariance matrix of X, and they define the new principal axes. By retaining only the top principal components, PCA reduces dimensionality while maintaining the most important variance in the data [83].

2.5.2.2 Support vector regression

SVR is a supervised learning algorithm designed for predicting continuous target variables based on a set of input features. Similar to other support vector machines, SVR aims to identify a hyperplane in a high-dimensional feature space that best represents the data while minimizing prediction errors (eq. 12 - 13):

$$\min_{\boldsymbol{w},b,\xi_i,\xi_i^*} \frac{1}{2} \| \boldsymbol{w} \|^2 + C \sum_{i=1}^{n} (\xi_i + \xi_i^*) \tag{12}$$

Subject to:

$$
\begin{aligned}
& y_i - (\boldsymbol{w}^\top \boldsymbol{x}_i + b) \leq \epsilon + \xi_i \\
& (\boldsymbol{w}^\top \boldsymbol{x}_i + b) - y_i \leq \epsilon + \xi_i^* \\
& \xi_i, \xi_i^* \geq 0, \qquad i = 1, \ldots, n
\end{aligned} \tag{13}
$$

where $\boldsymbol{w}$ is the weight vector, C is a regularization parameter controlling the trade-off between margin width and error, b is the bias term, $\boldsymbol{\epsilon}$ defines the tolerance margin, ξ_i and ξ_i^* are slack variables that allow some violations beyond ϵ, $\boldsymbol{x}_i$ and $\boldsymbol{y}_i$ are the input features and target values, respectively.

This approach employs an ϵ-insensitive loss function, which sets a tolerance margin for errors – smaller ϵ values lead to stricter tolerance and potentially more support vectors [84]. To capture non-linear relationships, SVR utilizes kernel functions that project the input data into a higher-dimensional space. Commonly used kernels include the polynomial kernel, which computes the inner product of input vectors raised to a power, and the radial basis function kernel, which measures the exponentiated squared Euclidean distance between input vectors, creating a smooth, non-linear decision boundary.

2.5.2.3 Convolution neural networks

A CNN is a type of supervised artificial neural network designed for tasks such as image classification and pattern recognition. It is particularly effective for processing image-like data structures, making it well-suited for analyzing HDEMG electrode grid images. CNNs leverage two fundamental principles: translational invariance, which enables the detection of features regardless of their spatial position, and compositionality, where simpler features combine to form more complex patterns [85]. These properties enable CNNs to efficiently extract spatial representations from structured data. CNNs typically use backpropagation to iteratively adjust the model's weights while minimizing prediction errors.

A CNN architecture typically consists of three main components [86]:

1. Convolution: learnable filters slide across the input data to detect spatial features, such as textures or activity patterns in EMG signals.
2. Activation: non-linear functions (e.g., ReLU) are applied to the convolved outputs to extracted features, introducing complexity into the learned representations.

3. Pooling: a downsampling operation, such as max pooling is used to reduce dimensionality while retaining the most significant information, improving efficiency.

2.6 Neuromuscular disorders

Neuromuscular disorders encompass a range of conditions that impair the function of muscles and the nerves controlling them, leading to various motor deficits. Among others, two notable examples are stroke and SCI, both of which can affect upper and lower MNs, resulting in distinct clinical manifestations.

2.6.1 Spinal cord injury

SCI results from damage to the spinal cord, leading to motor and sensory impairments caused by disrupted ascending and descending neural pathways. Causes of SCI include trauma, disease, or congenital conditions [87].

The severity and consequences of SCI depend on the level and extent of the damage, resulting in complete (no motor or sensory function below the injury) or incomplete (partial preservation of function) injuries. Clinical manifestations of SCI vary widely, including muscle weakness, sensory loss, involuntary muscle activation, and changes in motor control. Neuroplasticity may support partial recovery through the reorganization of spared neural pathway, particularly in cases of incomplete SCI [88, 89]. However, prolonged SCI often leads to muscle atrophy and morphological changes that affect force production and motor performance [90].

EMG enables quantifiable assessment of neuromuscular adaptations following SCI. EMG amplitude serves as a key indicator of muscle weakness and recovery [91-93]. While raw EMG signals can assess muscle activation presence or absence, EMG features such as RMS are often used to quantify activation levels. However, since EMG amplitude does not scale linearly with muscle force and varies highly across individuals and muscles, normalization to maximal EMG is commonly used for inter-subject comparisons.

Beyond amplitude-based metrics, frequency-domain analyses further reveal altered MU synchronization post-injury. Intra-muscular coherence in the β-band (15–30 Hz) is reduced in individuals with SCI, particularly in the tibialis anterior, and is associated with muscle weakness, gait impairments, and spasticity [94]. However, coherence measures are sensitive to experimental variables such as electrode placement [95] and signal preprocessing choices, including filtering and rectification [96, 97].

SCI also alters MU recruitment and firing properties. Studies report a reduced number of active MUs and larger MU sizes in both lower limb and hand muscles post-SCI [98], [99]. Changes in MU firing rates [100] as well as recruitment and de-recruitment thresholds [41] further highlight the impact of SCI on neuromuscular control. These changes contribute to impaired force production and modulation, affecting movement execution and coordination.

2.6.2 Stroke

Stroke results from an interruption of blood supply to the brain, leading to neuronal damage due to ischemia or hemorrhage. Depending on the affected region, stroke can impair both upper and lower MNs, causing a wide range of motor deficits, including muscle weakness, abnormal muscle tone (spasticity or flaccidity), and loss of voluntary motor control. While some recovery is possible through neuroplasticity, motor impairments often persist due to disrupted corticospinal and sensorimotor pathways [101].

CMC has become a widely used tool for investigating the functional coupling between cortical and muscular activity, particularly in the context of post-stroke motor dysfunction. CMC is typically observed in the β frequency band (15–30 Hz) reflecting the functional coupling between cortical and muscular activity particularly during sustained, steady-state muscle contractions, such as isometric movements in upper [22, 102] and lower limbs [103]. In individuals post-stroke, CMC is often reduced or altered, particularly in the paretic limb, indicating impaired corticospinal drive and sensorimotor integration [104], [49], [103]. Decreased beta-band coherence has been linked to deficits in voluntary movement and fine motor control [105], while increased low-frequency CMC (≤10 Hz) in some cases may reflect compensatory neural strategies or abnormal neural synchronization [106]. Additionally, changes in CMC over time can serve as a marker of neuroplasticity and functional recovery following stroke. Studies have shown that CMC peak increases with motor rehabilitation, suggesting the restoration of corticospinal connectivity [102, 107].

Given its ability to quantify sensorimotor connectivity, CMC is a valuable tool for assessing stroke-related motor impairment and monitoring recovery progress. However, methodological considerations such as electrode placement, EMG preprocessing, and task specificity must be carefully addressed to ensure reliable measurements. Most recent research has begun to investigate CMC between cortical activity and MU behavior, with evidence suggesting that CMC

analysis at the MU level enables more accurate estimation of corticomuscular delays [108, 109]. This emerging direction in CMC research holds promise, particularly for applications in stroke rehabilitation.

2.6.3 Clinical evaluation

Clinical evaluation of neurological impairments such as stroke and SCI uses standardized assessment tools to gauge motor and sensory deficits, spasticity, and functional mobility. These evaluations are efficient tools for physiotherapists assessing the level of injury, choosing individualized rehabilitation strategies and monitoring patient progress. Although these assessments are often subjective, they are easily implemented in clinical environments and, unlike other methods discussed in this thesis, do not require expensive equipment.

2.6.3.1 American Spinal Injury Association Impairment Scale

The American Spinal Injury Association (ASIA) developed the International Standards for Neurological Classification of Spinal Cord Injury, which includes the ASIA Impairment Scale [110]. This tool assesses the severity of SCI by evaluating motor and sensory functions across key muscle groups and dermatomes. Motor strength is graded on a scale from 0 (no muscle contraction) to 5 (normal strength), while sensory function is assessed for light touch and pinprick sensations. AISA scale categorizes injuries from Grade A (complete injury with no motor or sensory function preserved below the level of injury) to Grade E (unimpaired motor and sensory function).

2.6.3.2 Manual Muscle Testing (MMT)

MMT is a widely used clinical method for assessing muscle strength. Clinicians apply resistance to specific muscle groups and grade strength on a scale from 0 (no contraction) to 5 (normal strength) [111]. MMT is integral in evaluating patients with neurological impairments, including those resulting from stroke and SCI.

2.6.3.3 Modified Ashworth Scale (MAS)

MAS measures muscle spasticity by assessing resistance during passive muscle stretching. Spasticity, characterized by increased muscle tone, is common in conditions like stroke and SCI. The MAS grades spasticity from 0 (no increase in muscle tone) to 4 (rigid in flexion or extension) [112], offering a simple and

quick assessment to inform treatment strategies aimed at reducing spasticity and improving functional outcomes.

2.6.3.4 Functional Ambulation Category (FAC)

FAC evaluates a patient's walking ability, ranging from 0 (non-functional ambulation) to 5 (independent ambulation) [113]. It considers the level of support required and the patient's independence during ambulation. The FAC is particularly useful in stroke rehabilitation, providing insights into a patient's mobility status and helping to set realistic goals for gait training.

2.6.3.5 Fugl-Meyer Assessment (FMA)

FMA is a comprehensive, stroke-specific tool that evaluates motor functioning, balance, sensation, and joint functioning in patients with post-stroke hemiplegia [114]. It is divided into multiple domains, with the motor section assessing movements, reflexes, and coordination. The FMA is widely recognized for its reliability and validity, serving as a gold standard for measuring sensorimotor recovery in stroke patients and guiding rehabilitation interventions.

3 Aims and scope

The aims of this thesis are to investigate the alterations in the neuromechanics of ankle dorsi-/plantarflexor muscles, specifically the TA and soleus SOL, caused by SCI and stroke. Additionally, this work aims to explore how HDEMG can enhance ankle joint torque estimation by incorporating neurophysiological data and spatial distribution of muscle activation. The specific aims of each study are:

- ***Study I:*** Investigate how different EMG-derived inputs influence ankle joint torque prediction in the sagittal plane during both isometric and dynamic tasks using SVR. Specifically, torque prediction performance was compared across intra-session, inter-subject, and inter-session conditions using four EMG input modes: bipolar EMG, HDEMG, PCA-reduced HDEMG, and CNN-extracted HDEMG features.
- ***Study II***: evaluate the feasibility of using a computationally generated CST pool to simultaneously estimate physiological MU parameters and ankle joint torques during isometric and isokinetic dorsiflexion. By comparing torque estimation based on experimental EMG versus CST-derived neural drive, this approach aims to improve the neurophysiological fidelity of NMS models, particularly in isokinetic conditions.
- ***Study III***: Examine neurophysiological changes associated with SCI in key ankle dorsi-/plantarflexor muscles during sub-maximal voluntary isometric contractions in high-functioning individuals with incomplete paraplegia (SCI). Specifically focusing on differences in

muscle-level EMG parameters across both time and frequency domains, as well as MU characteristics.

- ***Study IV***: Investigate MU-level CMC in the lower limb, addressing the limited understanding of polysynaptic corticospinal projections and the impact of stroke-related connectivity disruptions. By analyzing EEG alongside EMG-derived CSTs and bipolar EMG in both able-bodied individuals and those with chronic stroke, we compare corticomuscular coupling across different representations of neural drive.

4 Methods

The methods for HD-EMG data collection and decomposition were consistent across multiple studies and are detailed in Sections 4.1 and 4.2. Other methods varied by study and are presented separately for each study.

4.1 HDEMG data collection

For Studies I - III, HD-EMG data were recorded at 2048 Hz and amplified using the Quattrocento biological signal amplifier (OT Bioelettronica, Italy). In Study IV, data were collected with the Muovi+ system (OT Bioelettronica, Italy) at a 2 kHz sampling rate.

Electrode grid placement was consistent across studies for TA (13×5, 8 mm inter-electrode distance, IED) and gastrocnemius medialis (8×8 grid, 10 mm IED) muscles. Additional grids varied by study: in Study I, an 8×8 grid with 10 mm IED covered SOL, and 8×4 grids with 4 mm IED were used for the gastrocnemius lateralis and peroneus longus. In Studies II and III, SOL was recorded with an 8×4 grid with 10 mm inter-electrode distance. In all cases the electrodes were positioned over the muscle belly, with the skin prepared beforehand by shaving and cleaning with an alcohol wipe.

For all studies involving isometric contractions, participants followed a trapezoidal torque profile with three phases (Figure 4.1): a linear ascent, a plateau, and a descent, guided by visual feedback. The rate of force development for both the ascent and descent phases was normalized to the maximum voluntary contraction (MVC). Participants were allowed to practice the task until confident in task execution.

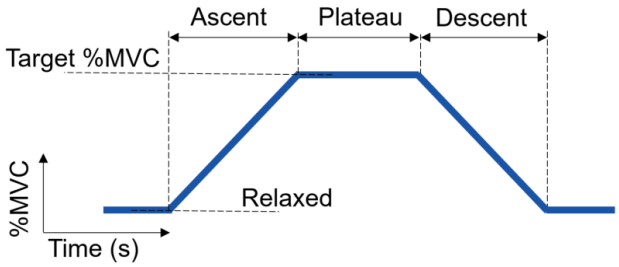

Figure 4.1 Trapezoid profile provided to participants as visual feedback. The profile starts at the relaxed position and ramps up to the plateau at a predefined rate (measured as percentage of maximum voluntary contraction per time, %MVC/s) to the target level of contraction (%MVC).

4.2 HDEMG data decomposition

MU decomposition was performed in Studies II–IV using the same pipeline. Monopolar HD-EMG signals were first band-pass filtered (20–500 Hz) and decomposed using the CKC method [32] implemented in DEMUSE software (version 6.0; University of Maribor, Slovenia). The identified MU spike trains were then visually inspected and manually refined following the guidelines by Del Vecchio et al. [115]. Only spike trains with a pulse-to-noise ratio above 30 [8] and at least 10 firing events within the analyzed time segment were included in the final analysis.

4.3 Study I

4.3.1 Participants

A total of twelve non-disabled participants with no history of neurological disorders or recent lower limb injuries were recruited for the study. The study consisted of two separate sessions: an isometric session and a dynamic session. The isometric session included five participants (two females, age 28.6 ± 5.4 years, height 169.0 ± 8.9 cm, weight 64.6 ± 16.1 kg), and the dynamic session involved seven participants (three females, age 31.6 ± 7.1 years, height 168.0 ± 7.8 cm, weight 67.6 ± 12.5 kg).

All experimental sessions were conducted at the Promobilia MoveAbility Lab, with approval from the Swedish Ethical Review Authority (2020-02311). All subjects provided written consent prior to data collection.

4.3.2 Experimental protocol

During data collection, HD-EMG signals were recorded from TA, SOL, gastrocnemius medialis and lateralis, and peroneus longus muscles of a randomly selected leg.

Isometric Contraction Protocol. Participants performed five sub-maximal isometric dorsiflexion and plantarflexion contractions plateauing at target levels of 30%, 50%, and 70% of MVC at four ankle angles (15° and 7.5° plantarflexion, neutral, and 10° dorsiflexion), totaling 24 trials per participant. Torque was measured with an isometric ankle dynamometer (OT Bioelettronica, sampling frequency 100 Hz). MVC was determined at each ankle position through three five-second maximal contractions, separated by one-minute breaks. The trapezoidal torque profile consisted of a 5 s ascent, 4 s plateau, and 5 s descent, with 10 s rest between repetitions.

Dynamic Task Protocol. Participants performed six dynamic tasks while HDEMG, marker trajectories, and ground reaction forces were recorded simultaneously. The marker data were acquired using a motion capture system (Vicon, 100 Hz sampling rate) and ground reaction forces were measured using a force plate (AMTI, 100 Hz sampling rate). Tasks included heel rises (parallel and wide stance), stance phase of gait, stepping onto/off an 18-cm platform, and a single-leg forward/backward reach task. Movements were performed at a self-selected pace in a randomized order.

4.3.3 Data processing

Ankle torque data was processed differently for isometric and dynamic protocols:

- *Isometric protocol:* Torque data from the dynamometer were normalized to MVC values and smoothed using a 500 ms moving average window with a 250 ms step size.
- *Dynamic protocol:* Ankle torque and plantar-/dorsiflexion angle were computed using inverse kinematics and inverse dynamics. Angular velocity was derived as the derivative of ankle angle. Torque was normalized to the subject's maximum torque across trials and smoothed with a 125 ms moving average window with 62.5 ms step size.

HDEMG data were band-pass filtered (20–500 Hz), with noisy channels interpolated from neighboring electrodes. Data were split into training (80%) and test (20%) sets for each of the four datasets:

- *HDEMG:* Rectified and smoothed using a moving average filter.
- *Bipolar EMG:* A single-differential signal was computed from two electrodes (20 mm apart), rectified, and smoothed.
- *HDEMG PCs:* PCA was applied separately to training and test sets. Three principal components per grid were selected based on explained variance.
- *HDEMG CNN:* A CNN was trained on the HDEMG training dataset. The trained model was then applied to the test set for feature extraction.

For dynamic tasks, each dataset was concatenated with ankle angle and angular velocity before applying the same moving average filtering used for torque processing.

4.3.4 ML algorithms

This study used two ML algorithms: CNN for feature extraction from HDEMG data and SVR for torque prediction. Both algorithms were implemented in Python 3.7 using Keras and scikit-learn.

The CNN architecture included one convolutional block (convolution, batch normalization, activation, max pooling, and dropout), followed by two fully connected layers and a regression layer. Each HDEMG electrode grid was treated as an image channel. Hyperparameters were optimized using grid search, varying node count (8, 32, 64, 128, or 256), learning rate (0.001 or 0.0001), and dropout rate (0, 0.2 or 0.4). Training was conducted up to 500 epochs, with early stopping if loss stagnated for 20 epochs. CNN features were extracted by removing the final fully connected layer, with the extracted features subsequently forwarded to the SVR.

The ϵ-SVR algorithm ($\epsilon = 0.01$) with an RBF kernel was used for 100 ms look-ahead torque prediction. In the isometric protocol, SVR was trained on the four EMG datasets described in section 4.3.3 with measured torque as the ground truth. In the dynamic protocol, ankle angle and velocity were added as kinematic features.

4.3.5 Performance evaluation

The agreement between measured and predicted ankle torque was assessed using root mean squared error normalized to the min-max of the torque (NRMSE).

The prediction results were assessed in three cases:

- *Intra-session*: Training and test data were from the same trial of the same subject, using five-fold cross-validation.
- *Inter-subject:* The test set was a trial from one subject, while the training set consisted of corresponding trials from all other subjects (n-fold cross-validation, where n – number of subjects).
- *Inter-session:* For isometric contractions, the test trial was excluded from the training set, which included all other trials of the same subject (k-fold cross-validation, where k – number of trials). For dynamic tasks, similar movements were used for training and testing (e.g., wide heel rises trained on narrow heel rises; stepping up/down trained on stepping down/up).

SVR prediction latency was measured in the intra-session case using only EMG features, assessing feasibility for real-time applications. This was tested on a PC with an Intel Core i7-9750H CPU and 32 GB RAM.

4.3.6 Statistical analysis

Wilcoxon signed-rank test was used to assess differences between EMG datasets in the isometric protocol, with a Bonferroni-corrected significance level ($\alpha = 0.008$) to reduce the risk of type I error. Statistical analysis was not performed for the dynamic task protocol due to the small sample size (n = 6 for stance, n = 7 for other movements).

4.4 Study II

4.4.1 Experimental protocol

Five participants (3 female; age: 52.4 ± 10.5 years; height: 173 ± 8.8 cm; weight: 90.9 ± 13.8 kg) with no history of neurological disorders or ankle injuries were recruited. The participants were seated, securely strapped, with the knee fixed at 60° flexion (Figure 4.2). They were asked to perform isometric and con-/eccentric isokinetic dorsiflexion tasks. The ankle was fixed at 10° dorsiflexion, neutral (0°), or 15° plantarflexion for isometric tasks, while isokinetic trials ranged from 15° plantarflexion to 10° dorsiflexion at 5°/s, 25°/s, or 50°/s. Trial order was randomized; each isometric condition was repeated three times, and each isokinetic condition five times. Prior to isometric and isokinetic trials, MVC was measured by two 3-second maximal contractions per position, with one-minute rests in between. Isometric tasks followed a trapezoidal torque profile,

ascending at rates of either 4% or 10% MVC/s to a 4-second plateau at 10%, 20%, or 50% MVC followed by a descent phase at the same rate. In isokinetic trials, no visual feedback was provided, but participants were asked to avoid maximal exertion.

Figure 4.2 Seating position during data collection for Study II.

HDEMG electrodes were placed over the TA, SOL and gastrocnemius medialis muscles. Torque and ankle position were recorded at 2000 Hz with isokinetic dynamometer (IsoMed 2000, D&R Ferstl GmbH, Germany), synchronized with HDEMG via a trigger.

Participants provided written informed consent, and the study was approved by the Swedish Ethical Review Authority (2020-02311).

4.4.2 Data processing and modeling approach

Dynamometer signals were low-pass filtered at 6 Hz and corrected for the offset caused by the weight of the shank and foot. HDEMG signals were processed separately to extract either EMG envelopes (for SOL and gastrocnemius medialis) or MU spike trains (for TA). For EMG envelopes, HD-EMG signals were band-pass filtered (10–500 Hz, second-order Butterworth). Noisy channels were visually identified and removed. Signals from the soleus and gastrocnemius medialis were averaged across each electrode grid, full-wave rectified, and low-pass filtered (4 Hz, second-order Butterworth). Envelopes were then normalized to the maximum MVC across all ankle positions per muscle and participant. MU spike trains from the TA were obtained following the process described in section 4.2.

The preprocessed data was used as the neural drive input to the model. The proposed modeling framework consists of two components (Figure 4.3): (1) a MU pool model estimating neural drive from a synthetic MU pool and (2) a calibrated musculoskeletal model estimating ankle joint torque.

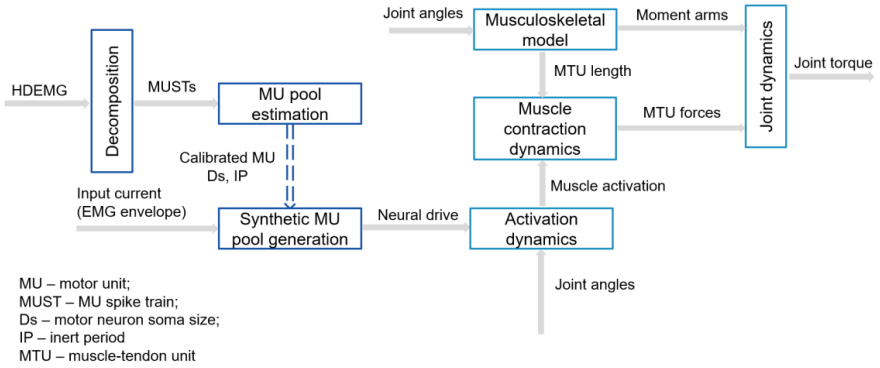

Figure 4.3 Proposed modelling pipeline for Study II, including MU pool model (left side) and the neuromusculoskeletal model (right side).

4.4.2.1 MU Pool Model

The MU pool model, adapted from Duan et al. [116], involves three key steps: estimating common synaptic input, simulating MN firing, and determining MN parameters to estimate MU pool behavior (see section 2.4). Common synaptic input, representing net synaptic input, is derived by low-pass filtering the CST of recruited MUs detected via HD-EMG decomposition. A modified LIF model simulates MN firing based on soma size D_s and inert period IP parameters, optimized using a genetic algorithm (population size = 50, elite count = 3, crossover rate = 0.8, tolerance = 10^{-6}) to match experimental spike train discharge rates. The complete MU pool (modeled with 400 MUs in TA) is reconstructed using membrane time constant $\tau = 2.3 \cdot 10^{-9}/D_s^{1.48}$ and the membrane resistance $R = 5.1 \cdot 10^{-5}/D_s^{2.43}$ [117], resting membrane potential of 0 mV, and the spike threshold of 27 mV. Model parameters were estimated from 10%, 20%, and 50% MVC trials and extrapolated to the full MN pool using nonlinear fitting.

4.4.2.2 Neuromusculoskeletal Model

An open-source EMG-driven framework (CEINMS [7]) was used to estimate NMS dynamics, consisting of four components: activation dynamics, contraction dynamics, musculoskeletal model, and joint dynamics (Figure 4.3).

Activation dynamics converts neural drive into muscle activation. Neural drive sources include EMG envelopes of TA, gastrocnemius medialis and SOL and, additionally for TA, both filtered CSTs from the modelled or decomposed MU pool. Activation is modeled with recursive filtering and electromechanical delay. The resulting activation is then used as input to contraction dynamics that uses a Hill-type model incorporating force-length, force-velocity, and passive force relationships to compute muscle forces. These parameters are used in a scaled and simplified OpenSim *leg39* model [118], including only the TA, SOL, and gastrocnemius muscles, with the knee and hip fixed and the ankle restricted to dorsi-/plantarflexion. The model's estimated muscle forces and moment arms are then used to calculate ankle joint torque.

Model parameters (C1, C2 (eq. 9), A (eq. 10), and maximal isometric force of each muscle) were calibrated via simulated annealing, minimizing the error between predicted and measured torques. The calibration was performed for each trial using data from all but one available repetitions.

4.4.3 Performance evaluation

To evaluate model performance, three neural drive inputs were compared: EMG-driven, decomposed MU CST-driven, and MU pool-driven models. Since the framework involves two steps, performance was assessed separately at each step. We first assessed the MU pool estimation of neural drive and then evaluated the complete NMS model's ability to estimate ankle joint torque.

The first step aimed to assess the consistency of MU pool neural drive estimations under different conditions. MN parameters were estimated in two configurations: (a) based on the first repetition of all isometric trials at a single ankle position, and (b) based on the first repetition of all isometric trials across multiple ankle positions. The resulting neural drives from MU pool CST estimates across all trials were compared using the coefficient of determination (R^2).

The second step assessed torque prediction accuracy using different neural drive inputs (EMG envelope, CST, and CST pool) by comparing predicted and measured ankle torque. First the NMS model was calibrated using two of three repetitions per trial using EMG envelopes as input. The remaining unseen repetition was then used to evaluate torque estimations based on the three neural drive inputs, with accuracy quantified by the NRMSE, normalized to the maximum torque of each trial. Statistical differences in torque estimation

among models were assessed using the related-samples Wilcoxon signed-rank test ($\alpha = 0.05$).

4.5 Study III

4.5.1 Participants

Twenty participants with sub-acute or chronic incomplete SCI (9 females, age 58.9 ± 10.9 years, height 163.9 ± 3.5 cm, weight 79.8 ± 18.2 kg, injury duration: median 2.2 years, range 0.6–17 years) and 17 control participants (10 females, age 53.1 ± 12.4 years, height 170.2 ± 8.4 cm, weight 69.5 ± 13.1 kg) were recruited. The SCI group was a subset of participants from study by Butler Forslund et al. [119]. Inclusion criteria ensured that SCI participants could complete the protocol but had reduced plantarflexor strength: (i) MMT results between 2 and 4 and (ii) MAS spasticity below 4. Controls were included if they had no neurological disorders or recent lower limb injuries.

All SCI participants underwent clinical evaluations using the International Standards for Neurological Classification of SCI and were classified as ASIA grade D, meaning at least half of the key muscles below the injury level retained function. Six SCI participants exhibited plantarflexor hyper-resistance (MAS 1–3). Measurements were taken from the weaker side in asymmetric motor function cases, the side with poorer sensory function in symmetric cases, and a randomly selected side in controls.

Data collection was conducted at Promobilia MoveAbility Lab (Stockholm, Sweden). The study was approved by the Swedish Ethical Review Authority (2020-02311, 2020-07067, and 2022-00629-02). All participants provided written informed consent.

4.5.2 Experimental protocol

Participants performed isometric plantar- and dorsiflexion while seated with their knee fixed at 90° flexion and ankle at 0° (neutral position). Ankle force dynamometer under the forefoot measured both tension and compression at 100 Hz (OT Bioelettronica, Italy). HDEMG electrode grids were placed over TA and SOL muscles. MVC was determined from the peak force in two 3-second repetitions, separated by a one-minute rest. Participants then followed visual torque feedback to perform four repetitions of a trapezoidal torque profile with 5 s ascent, 4 s plateau at 20% or 50% MVC, 5 s descent, and 10 s rest.

4.5.3 Data processing

Dynamometer data were low-pass filtered at 10 Hz and divided into four repetitions, each segmented into ascent, plateau, and descent phases. The torque coefficient of variation (CoV_{TRQ}) was calculated for the plateau to assess sustained force variability at each MVC level.

HDEMG signals were band-pass filtered (20-500 Hz). Noisy channels were manually removed. EMG amplitude was analyzed as normalized root mean square ($NRMS_{EMG}$) by normalizing the RMS of each electrode to its MVC value. The mean $NRMS_{EMG}$ for all electrodes and repetitions was computed per muscle and participant. The co-contraction index (CCI, eq. 14) for the antagonist muscle pair (TA and SOL) was calculated at each time point as:

$$CCI(t) = \frac{2a_S(t)}{a_S(t) + a_L(t)} \tag{14}$$

where a_S and a_L represent the $NRMS_{EMG}$ of the less and more active muscles, respectively.

Monopolar HDEMG signals were decomposed as described in section 4.2. MU ISIs were calculated as the time between consecutive firings, with physiologically unrealistic firings and de-recruitment periods removed (33.3 ms ≤ ISI ≤ 200 ms) [36, 120]. The coefficient of variation of ISI (CoV_{ISI}) was computed during the plateau phase, and MU discharge rates were estimated for ascent, plateau, and descent phases.

To estimate MU synchronization in the frequency domain, data from the plateau phases of four repetitions (16 s total) were used to calculate intramuscular coherence. Six randomly selected MUs were grouped into two CSTs. Power spectral density was calculated using Welch method and used to calculate intramuscular coherence. The process was repeated for up to 100 random permutations, and the median coherence value was taken for each frequency band (δ, α, β, γ). In time domain, MU synchronization was quantified with the common input strength (CIS) index. This was computed by calculating the cross-correlogram of two CSTs and identifying the peak using the cumulative sum method. The CIS was calculated as the peak count divided by the recording length.

4.5.4 Statistical analysis

The outcome parameters in this study include CoV_{TRQ}, $NRMS_{EMG}$, CCI, MU discharge rates, recruitment and de-recruitment thresholds, CoVISI, MUAP amplitude, CST coherence, and CIS.

For MU-related parameters (discharge rates, recruitment/de-recruitment thresholds, CoVISI, and MUAP amplitude), statistical significance was assessed using robust linear mixed models in R. The group was treated as a fixed effect, and subjects and the number of identified MUs per subject were treated as random effects. P-values were evaluated using the *modelsummary* library, with significance set at $p < 0.05$.

For other parameters, medians were computed at 20% and 50% MVC for TA and SOL across all participants. For EMG parameters, medians were calculated from all HDEMG channels and movement repetitions. When normal distribution assumptions were violated (verified by the Shapiro-Wilk Test), the Mann-Whitney U test ($p < 0.05$) was used for statistical significance. Otherwise, independent samples t-tests ($p < 0.05$) were applied.

4.6 Study IV

4.6.1 Participants

The study included 20 participants, consisting of 10 participants with chronic stroke (6 female, mean age 60 ± 7.2 years; MMT: median 4, MAS: 2, FAC: 5, FMA: 35.5) and 10 controls (8 female, mean age 64 ± 8.3 years). Before participation, participants in the stroke group underwent clinical assessments including MMT, FAC, MAS, and FMA tests, to confirm eligibility. All stroke participants had unilateral motor paresis resulting from ischemic or hemorrhagic stroke. To be eligible, stroke participants needed to have an mini-mental state examination score above 21, be able to sit upright for 60 minutes (with or without assistance), and have a TA muscle strength of at least 3 on the MMT scale. Exclusion criteria for stroke survivors included a history of secondary strokes, severe communication issues, or any medical or psychological conditions that could interfere with study compliance. Additional exclusions included neurological diseases, psychiatric disorders, epilepsy, alcoholism, substance abuse, current pregnancy, pacemaker or deep brain stimulator implants, and involvement in other clinical trials. Control participants were screened to confirm the absence of neurological, psychiatric,

or musculoskeletal disorders and were matched with stroke survivors for age and sex.

4.6.2 Experimental protocol

The protocol involved isometric dorsiflexion tasks during which participants were seated with their knee at 90° flexion and the ankle in a neutral position. Participants first performed MVC tasks, followed by submaximal dorsiflexion tasks guided by visual feedback. MVC was determined as the maximum TA EMG envelope from three 5-second maximum isometric dorsiflexion trials, each separated by 1-minute rests. Submaximal tasks followed trapezoidal force profiles with force ascent and descent at 4% MVC/s, with 20-second plateaus at 20% and 40% MVC. For each MVC level, participants completed five repetitions with 30-second rest intervals. One control and two stroke participants could not maintain 40% MVC for 20 seconds, so their trials were modified to include ten repetitions with 10-second plateaus. Stroke participants performed tasks on both paretic and non-paretic sides, while control participants performed tasks using a randomly selected side.

HDEMG and EEG data, synchronized via a LabView trigger, were recorded during the isometric tasks. HDEMG was recorded from TA and SOL muscles, but only TA data was used for analysis. EEG was recorded using a g.USBamp system with a gamma-cap (1.2 kHz sampling rate), and electrodes were positioned over the motor cortex according to the 10–10 system (Figure 4.4).

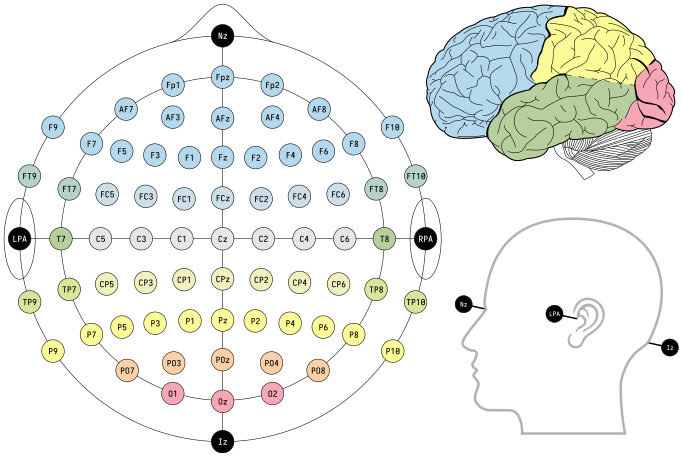

Figure 4.4 International 10-10 EEG electrode placement system along with the corresponding areas of the cortex (Krol, L. R. (2020). Wikimedia Commons [CC0 1.0])

Data collection took place at the Hong Kong Polytechnic University, approved by the Human Subjects Ethics Sub-Committee (HSEARS20210320003) and the Joint Chinese University of Hong Kong - New Territories East Cluster Clinical Research Ethics Committee (2022.309-T). All participants gave written informed consent.

4.6.3 Data processing

The HDEMG signals were processed to extract CST, and bipolar EMG for CMC analysis. The signals were band-pass filtered at 20 – 500 Hz. One channel at the center of the electrode grid was selected for bipolar EMG representation. The decomposed MUs were only kept for further analysis if they were continuously firing during the plateaus of all five trials. ISIs were calculated as the time between consecutive firings, while MU discharge rates were computed as the inverse of ISIs. Recruitment thresholds were defined as the mean MVC level during the first five firing events of force ascent.

The MUs were then separated into coherent and non-coherent groups based on CMC characteristics. Coherent MUs were defined as those that (i) exhibit significant CMC peak values and (ii) have peak CMC at electrodes covering the contralateral sensorimotor cortex [108]. We adopted this definition for the control group; however, in stroke participants, the peak CMC often shifts toward the ipsilateral (contralesional) motor cortex, so only the first criterion (significant CMC peak) was used for the stroke group. Significant CMC was

determined using the confidence level $C = 1 - \frac{\alpha}{\beta - 1}$, where α is the significance level (0.05) and β is the number of epochs. CSTs were then computed for each MU group by summation of the spike trains of all active MUs.

EEG signals were band-pass filtered between 5–100 Hz and notch filtered at 50 Hz to reduce power line noise. The EEG data were then preprocessed with average rereferencing and independent component analysis (FastICA algorithm) to remove artifacts, such as eye movements, head movements, and EMG interference.

The CMC calculation pipeline was implemented using the Matlab FieldTrip toolbox (v. 20241025) [121]. EMG signals were downsampled to match the EEG sampling frequency and segmented into 1-second, non-overlapping windows for 1 Hz frequency resolution. Power and cross-spectral densities for CMC were computed via fast Fourier transform. CMC was computed between EEG and three types of EMG-derived signals: bipolar EMG (CMC_{EMG}), coherent MU CSTs (CMC_{coh}), and non-coherent MU CSTs (CMC_{ncoh}). Z-score normalization was applied for group comparison, and spatial entropy H (Eq. 15) was used to quantify CMC dispersion across EEG channels.

$$H = -\sum p(i) \log_2 p\,(i) \tag{15}$$

where $p(i)$ is the probability distribution of CMC at channel). Higher entropy values indicate more evenly distributed CMC.

Cross-covariance was used to estimate corticomuscular delays, with significant delays identified as the peak cross-covariance between EEG and muscle activity. Only positive delays were considered for descending corticomuscular analysis. CST-CST coherence was computed to evaluate common synaptic drive among MUs within coherent and non-coherent groups, using two randomly selected MUs from each group. Coherence was calculated in the δ band (0.5–4 Hz) and repeated for up to 100 permutations. Analysis required at least four MUs identified per participant.

4.6.4 Statistical analysis

To examine the relationship between MU parameters (discharge rate and recruitment threshold) and CMC, pairwise linear correlation analyses were performed. Comparisons of means of corticomuscular delays, CST-CST coherence, and entropy were performed using two different non-parametric tests:

- For within-group comparison (coherent vs. non-coherent MUs, and between non-paretic and paretic sides in the stroke group), the related-samples Wilcoxon signed-rank test was used.
- For between-group comparisons (e.g., control and stroke groups), the independent-samples Mann-Whitney U test was used.

A significance level of 5% ($p = 0.05$) was used for all tests.

5 Results and discussion

5.1 Ankle torque estimation

In this thesis, ankle joint torque estimation was explored through two distinct approaches: ML in Study I and NMS modeling in Study II. Both methods were driven by either HDEMG or conventional bipolar EMG data, and their performances of joint torque estimation were compared. In Study I, the primary advantage of HDEMG over bipolar EMG is additional spatial information it provides. This enables the extraction of salient spatial features from the EMG signal, which can improve torque estimation performance. Study II leveraged the HDEMG for the extraction of MU activity, enabling physiologically informed neural drive inputs within the NMS model. The results and implications are discussed in more detail for each study separately.

5.1.1 ML approach

Study I compared four types of EMG inputs (HDEMG, HD-EMG PCs, bipolar EMG, and CNN-extracted HDEMG features) for ML-based ankle torque prediction. In isometric conditions, HDEMG-derived inputs significantly improved torque estimation accuracy compared to bipolar EMG, especially in inter-subject and inter-session cases. However, in dynamic movements, torque prediction errors were higher across all EMG types. Notably, only the incorporation of kinematic features led to improved prediction accuracy, highlighting the influence of additional biomechanical information i.e., joint position and velocity in torque estimation (Figure 5.1).

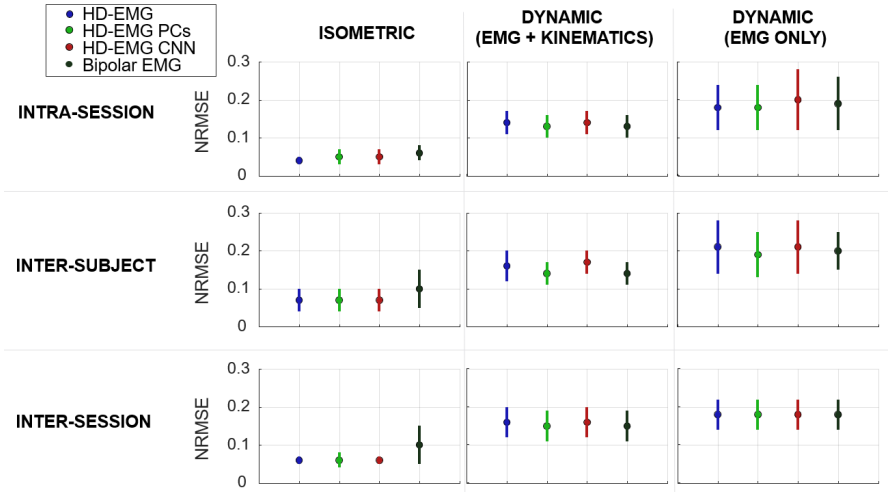

Figure 5.1 Means (dots) and standard deviations (lines) of the torque prediction results of the first study. The results of all movements in isometric protocol and dynamic protocol with and without additional kinematic features are shown for intra-session, inter-subject and inter-session cases.

For isometric movements, the ML model demonstrated significantly improved prediction accuracy when using HDEMG data compared to bipolar EMG, particularly for inter-session and inter-subject cases ($p = 0.01$ or less in all cases). This improvement reflects that the salient spatial features of muscle activation in the HDEMG data enables robust prediction of torque under controlled, isometric conditions. The HDEMG-derived datasets effectively captured subtle variations in muscle activation patterns that are essential for accurate torque estimation in static tasks. This finding aligns with previous research reporting superior prediction accuracy when using HDEMG over bipolar EMG in isometric conditions [24], where muscle activity is more predictable and less subject to the non-stationary effects seen in dynamic movements.

During dynamic movements, where signals are non-stationary and the muscle activation patterns become more complex, the prediction accuracy was comparable among the datasets. The ML model did not demonstrate consistent improvements in prediction accuracy when using HDEMG-derived data, and the overall torque estimation errors were larger and more variable than those observed in isometric contractions. This result can be explained by the dynamic nature of the movements, where muscles are not stationary relative to the electrode array, and their contributions to joint torque change depending on factors such as ankle and knee joint positions and movement velocity. The

increased variability in muscle recruitment strategy, along with nonlinear changes in muscle forces due to joint kinematics (driven by force–length and force–velocity relationships) can make it more challenging for HDEMG-based models to accurately predict torque, especially when relying solely on EMG inputs.

Muscle forces vary nonlinearly with changing joint kinematics due to the force–length and force–velocity relationships. The inclusion of kinematic data (joint position and velocity) significantly improved the performance of the ML model in dynamic torque prediction. This finding aligns with the results of Hajian et al. [77], who showed that the adding kinematic features enhanced torque prediction accuracy for elbow movements. As described in section 0, joint torque is inherently dependent on joint position and velocity. The addition of kinematic input data likely provided the necessary biomechanical context, reflecting changes in muscle force generation capabilities during dynamic movement. For example, variations in joint angles alter muscle lengths and moment arms, directly influencing the torque produced by the muscles. Therefore, relying solely on EMG data for dynamic torque prediction may be insufficient, as it fails to capture the critical effects of joint motion on muscle force production.

5.1.2 NMS modeling approach

Study II introduced a novel NMS modeling framework that integrates a synthetic MU pool to estimate physiological MU parameters while simultaneously predicting ankle joint torques during isometric and isokinetic dorsiflexion. The decomposed MU data were used to optimize motoneuron parameters and construct a synthetic MU pool, enabling neural drive estimation for the entire MU population. To evaluate robustness and transferability of the neural drive estimations from the MU pool model, we compared MU pool models calibrated using data from a single ankle position to those calibrated across multiple positions during isometric contractions. Additionally, to evaluate the accuracy of the whole modeling approach, we examined torque estimation performance between models driven by MU-derived neural drive and those driven by conventional bipolar EMG inputs. Although some discrepancies were observed in isometric torque predictions between the two approaches, isokinetic torque predictions remained comparable. These findings suggest that this integrative modeling approach may provide valuable insights into how neural drive influences musculoskeletal function, particularly in dynamic conditions.

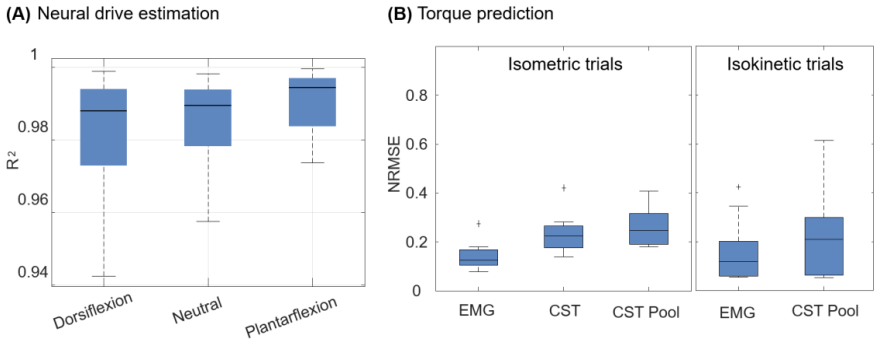

Figure 5.2 (A) Summary of the agreement across participants and trials between neural drives estimated by CST pool models calibrated either across all ankle positions or individually at each ankle position. The indicated ankle position refers to the calibration condition. (B) Normalized root mean squared error (NRMSE) of torque estimations for isometric and isokinetic trials using EMG-driven, CST-driven, and CST pool-driven models.

This study demonstrated that neural drive estimates derived from the MU pool model were largely unaffected by whether calibration was performed at a single ankle position or across multiple positions during isometric contractions (Figure 5.2 A). This outcome supports the principle that MU discharge patterns are predominantly governed by muscle activation demands and external load, rather than variations in joint angle. Since the model is driven by MU firing events alone and does not incorporate MU action potentials, which can shift with muscle length due to changes in electrode positioning. This consistency across joint positions was expected. Notably, MU parameter estimation revealed a tendency for saturation at higher torque levels, especially during isokinetic trials, likely due to the restricted range of contraction intensities sampled (≤50% MVC). These observations highlight the importance of capturing a more evenly distributed set of MUs across the full spectrum of contraction intensities to improve model accuracy and the reliability of neural drive estimations, particularly when extending to higher force levels.

The use of a CST pool-driven approach in neuromusculoskeletal modeling offers a potential advantage by incorporating MU recruitment dynamics and firing behaviors typically oversimplified in conventional EMG-driven frameworks. However, in isometric conditions, torque predictions derived from the CST pool model exhibited higher errors than those from the EMG-driven model (Figure 5.2 B). This discrepancy may be attributed to incomplete representation of low-threshold MUs, calibration bias arising from EMG-based model optimization in CEINMS, and possible limitations in the normalization of synaptic input currents. In isokinetic contractions, both modeling approaches produced

comparable torque estimation errors, with overall accuracy reduced relative to isometric tasks (Figure 5.2 B) —likely reflecting the added mechanical and neuromuscular complexities of dynamic movement, including force-velocity interactions and varying muscle-tendon dynamics. Nonetheless, the CST-driven approach is motivated by the goal of providing a more physiologically representative neural drive estimation by incorporating MU recruitment and firing properties, which are often simplified in traditional EMG-driven approaches. The proposed modelling approach is able to achieve this across all subjects by successfully estimating the soma size ($Ds = 61.4 \pm 33.9\ \mu m$) and inert period ($IP = 95.2 \pm 24.2\ ms$) of the MUs in the pool. Although there are no studies on human TA soma size and *IP* estimation, we observed positive association between *Ds* and contraction intensity, which aligns with established neuromuscular principles, supporting the physiological relevance of these estimates. Although current limitations in parameter fitting and sensitivity were noted, particularly for *IP*, these results suggest that CST-driven approaches could enhance the physiological interpretability and personalization of neuromusculoskeletal models in future applications.

5.1.3 Limitations and alternative approaches

Both studies have limitations that affect the generalizability and accuracy of the findings. In Study I, the small and relatively homogeneous subject cohort (n = 5 for isometric and n = 7 for dynamic tasks) limits the broader applicability of the results. Additionally, the isometric protocol constrained the ankle joint to its mid-range of motion, potentially limiting the model's ability to accurately predict torque at more extreme joint positions. Although the study focused on evaluating different EMG input features rather than achieving the best prediction accuracy, the limited dataset may have hindered the performance of CNN. Expanding the dataset could improve model performance and allow the use of more complex machine learning algorithms, such as deep neural networks. Furthermore, HD-EMG recordings were limited to five ankle muscles; incorporating signals from additional lower limb muscles, along with joint kinematics, could further enhance robustness and predictive accuracy.

In Study II, a key limitation was the potential duplication of MUs across different ankle positions and contraction levels, which may have led to an overrepresentation of certain units when estimating the synthetic MU pool. Additionally, the optimization of MU pool parameters was restricted to MUs recruited at moderate torques (≤50% MVC). While this range captures the

majority of TA MUs, it excludes those activated at higher contraction levels. This constraint may compromise torque estimation accuracy at maximal effort levels. Expanding the calibration range to include higher contraction intensities could improve model accuracy and improve the torque prediction across the full spectrum of intensity.

One of the main findings of this thesis is that while ML methods are effective for torque prediction in static conditions, their performance are limited in dynamic scenarios due to absence of explicit physiological constraints, such as muscle force-velocity relationships and joint angle dependencies. On the other hand, the NMS modeling approach offers a more integrated representation of neural and mechanical function by incorporating MU firing properties into the modeling. This highlights the potential benefits of combining the strengths of both approaches in future work. A hybrid approach that integrates ML with MU-based modeling could offer significant improvements in torque estimation in dynamic tasks by leveraging the strengths of both approaches: the data-driven capabilities of ML alongside the physiological fidelity of MU-based model. One promising direction involves the use the physics-informed neural networks, which have demonstrated great potential in muscle force and joint torque estimation [122, 123]. By embedding biomechanical constraints and physiological knowledge into the learning process, such approaches could lead to more accurate prediction of torque in dynamic movements and offer deeper insights into underlying neuromuscular mechanisms.

5.2 MU parameter assessment in neuromuscular disorders

Studies III and IV in this thesis explore different aspects of neuromuscular control, with a particular focus on mechanisms of force modulation and corticospinal connectivity in both healthy and pathological conditions. Both studies use HDEMG to observe the MU behavior *in-vivo*, including recruitment, discharge properties, and corticospinal interactions that influence force generation and neural adaptations. Specifically, Study III examined neuromuscular adaptations following SCI, while Study IV focused on corticospinal connectivity at the MU level in individuals after stroke. Together, these studies provide novel insights into the complex interplay between neural drive and muscular output, demonstrating that alterations in MU recruitment strategies and connectivity patterns may serve as potential biomarkers for impaired or adaptive neural control of motor function.

5.2.1 Neuromuscular Adaptations After SCI

Study III explored neurophysiological adaptations in the TA and SOL muscles following SCI by analyzing EMG and MU properties during submaximal isometric contractions. Our findings reveal altered force generation and modulation strategies after SCI. Specifically, increased $NRMSE_{EMG}$, along with unchanged MU synchronization, reduced firing rate and lower recruitment thresholds, suggest notable changes in MU behavior. Additionally, indirect evidence indicates to an increased MU size (Table 5.1). Collectively, these results indicate a shift towards recruitment of larger MUs in both dorsi- and plantarflexor muscles, which may reflect compensatory adaptations to MU loss or reorganization following SCI.

Altered force generation strategies after SCI were evident from the increased normalized EMG amplitude ($NRMS_{EMG}$) in the SCI group, which did not correspond to elevated MU firing rates or greater MU synchronization (Table 5.1). Instead, the findings suggest that individuals with SCI compensate by recruiting either a greater number of MUs or larger MUs to generate force. This interpretation is supported by significantly higher MUAP amplitudes in the TA muscle, indicating that detected MUs were likely larger, consistent with previous studies reporting of similar adaptations in hand muscles post-SCI [35, 99]. Additionally, despite higher EMG amplitudes, SOL discharge rates were only reduced during recruitment, whereas TA discharge rates were lower across all movement phases, highlighting that the adaptations might be muscle specific.

We observed altered force modulation strategies after SCI, evidenced by significantly lower MU recruitment thresholds in both the TA and SOL. This finding contrast with previous studies on hand muscles which reported increased recruitment thresholds post-SCI [41], likely reflecting functional differences between lower limb and upper limb muscles. Despite these changes in recruitment threshold, no significant differences in MU synchronization were observed. This result contrasts with earlier studies showing reduced TA coherence during maximal voluntary contractions in individuals with SCI [94]. Discrepancies may arise from methodological differences, including coherence analysis approaches and trial durations. Overall, these findings emphasize the complexity of neuromuscular adaptations after SCI and highlight the need for future research incorporating additional methodologies, such as nerve stimulation, to more comprehensively characterize underlying mechanisms to support these findings.

Table 5.1 Summary of the results of Paper II. The parameters for dorsiflexion/tibialis anterior (DF/TA) and plantarflexion/soleus (PF/SOL) in SCI group are compared to the same parameters in the control group and p values are given for all statistically significant differences. The 20% and 50% refer to the percentages of maximum voluntary contraction of the plateau. N.S. – non-significant differences.

Parameter			Observation, SCI compared to control	
			DF/TA	PF/SOL
EMG	$NRMS_{EMG}$		Higher at 20% ($p = 0.003$)	Higher ($p < 0.001$)
	Co-contraction index, CCI		N.S.	N.S.
MU	Recruitment threshold		Lower at 50% ($p < 0.001$)	Lower (20% $p = 0.046$; 50% $p < 0.001$)
	MU discharge rate	Ascent	Lower ($p < 0.01$)	Lower (20% $p = 0.044$; 50% $p = 0.010$)
		Plateau	Lower (20% $p = 0.011$; 50% $p = 0.014$)	N.S.
		Descent	Lower (20% $p = 0.048$; 50% $p = 0.006$)	N.S.
	MUAP amplitude		Higher at 20% ($p = 0.046$)	N.S.
	Intramuscular coherence (all frequency bands)	Ascent	N.S.	N.S.
		Plateau	N.S.	N.S.
		Descent	N.S.	N.S.
	Synchronization Index, CIS		N.S.	N.S.

5.2.2 MN-Level Corticomuscular Connectivity in Stroke

This study provides a novel analysis of CMC at the MU level by simultaneously recording EEG and HDEMG during voluntary isometric contractions of the TA. Using MU decomposition, we examined corticospinal interactions with higher resolution than traditional muscle-level analyses, including the MU-level CMC assessment in individuals post-stroke. Our findings revealed no significant correlation between MU firing characteristics and CMC strength (Figure 5.3 A), suggesting that individual MN properties may not directly influence CMC.

Additionally, while no significant differences in corticomuscular delays or shared synaptic input were detected between coherent and non-coherent MN groups, the paretic side demonstrated distinct alterations. Finally, CMC topography (Figure 5.3 C) remained consistent across different EMG-derived signals, reinforcing the robustness of the observed patterns and highlighting the potential of MN-level analysis for investigating corticospinal coupling.

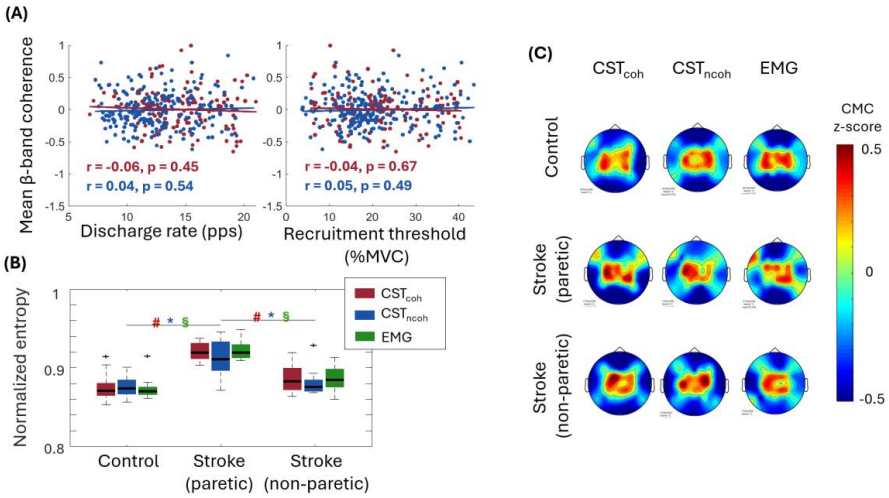

*Figure 5.3 Results of Study IV. (A) Correlation between motor neuron (MN) parameters and corticomuscular coherence (CMC) in the β frequency band for coherent and non-coherent MNs in the control group. Each dot represents an individual MN, and each subplot includes MNs pooled from all participants within the control group. p-values indicate the significance of the correlation, as quantified by the Pearson correlation coefficient (r). (B) Spatial entropy of EEG CMC for coherent MNs, non-coherent MNs, and EMG signals, assessed at 20% MVC across all subjects. Statistically significant differences between participant groups are denoted by # (coherent MNs), * (non-coherent MNs), and § (EMG). (C) Topographical maps show the mean EEG CMC z-scores at 20% MVC for coherent MNs, non-coherent MNs, and EMG. Each plot represents the average z-score distribution across all subjects within each group. All recordings were performed on the right side (7 control participants, 5 paretic, and 5 non-paretic limbs).*

We found that intrinsic MN firing characteristics alone do not determine the strength of CMC, as evidenced by the lack of correlation between MN parameters and CMC ($|r| \leq 0.06$ in all cases). This observation aligns with computational models suggesting that CMC arises from the interplay between cortical inputs and the collective oscillatory behavior of the MN pool rather than individual firing properties [124]. While previous studies have examined the contribution of MN discharge properties to CMC, our findings reinforce the notion that corticospinal coupling is predominantly shaped by broader network-level dynamics — including oscillatory interactions within cortical motor areas

and spinal interneuronal circuits — rather than the intrinsic properties of individual MNs. Moreover, we found no significant differences in corticomuscular delays or shared synaptic input between coherent and non-coherent MN groups, challenging the hypothesis proposed by Zheng et al. [108] that coherent MNs receive more direct corticospinal input. Although it has been suggested that coherent MNs reflect monosynaptic corticospinal pathways, our findings indicate that this suggestion may not fully apply to the TA muscle, a muscle primarily governed by polysynaptic pathways.

CMC results were robust across different modalities (CMC_{coh}, CMC_{ncoh}, and CMC_{EMG}), reinforcing the robustness and validity of MN-level CMC as a reliable measure of corticospinal interactions in both healthy and stroke-affected populations. Our topographic analysis revealed CMC peaks were predominantly localized in the central midline and adjacent parasagittal electrodes. Notably, the paretic side exhibited significantly higher spatial entropy compared to both the non-paretic side of stroke participants (at 20% MVC $p \leq 0.021$ for all EMG modalities) and the control group ($p \leq 0.001$ for all EMG modalities and contraction intensities), regardless of the EMG-derived CMC computation method used (Figure 5.3 B). These findings are consistent with previous studies on lower limb muscle CMC utilizing conventional EEG-EMG techniques, which have consistently identified the midline region as the primary site of corticomuscular interactions [125, 126]. The increased spatial entropy on the paretic side further supports the widely accepted view that stroke-induced neuroplasticity disrupts cortical synchrony, leading to greater variability in neural activation patterns. This loss of synchrony may impair the efficiency of motor command transmission, potentially contributing to the motor deficits observed in stroke survivors.

5.2.3 Unifying Perspectives

While HDEMG provides a powerful non-invasive tool for studying MU-level changes, its application in neuromuscular disorders presents several limitations. A primary constraint is the variability in MU decomposition accuracy, which can be influenced by factors such as electrode placement, individual muscle properties, and contraction conditions. This variability can be often exacerbated in individuals with neuromuscular disorders due to alterations in muscle morphology, increased fibrosis, or disruptions in excitation-contraction coupling. Additionally, the number of identified MUs can vary considerably across muscles and individuals, potentially introducing to biased estimates of MU characteristics in affected populations. HDEMG is also

inherently limited in its ability to capture muscle activity from deeper MUs, as surface electrodes primarily record signals from superficial muscle layers. This limitation is particularly relevant in conditions where deeper MUs may be preferentially affected, e.g. in amyotrophic lateral sclerosis or SCI. Furthermore, while MU discharge behavior can provide valuable insights into neural adaptations, it remains an indirect measure of underlying neural mechanisms, making it challenging to disentangle the relative contributions of cortical, spinal, and peripheral processes to observed changes in MU activity.

Future work could address these limitations by integrating HDEMG with complementary techniques such as electrical or magnetic stimulation may provide more direct assessments of MU recruitment properties and excitability. Combining HDEMG with functional neuroimaging modalities could also provide a more comprehensive evaluation of corticospinal adaptations in individuals with neuromuscular disorders. Moreover, advancements in signal processing and decomposition algorithms also hold promise for improving the reliability of MU identification, particularly in pathological conditions with irregular or complex MU firing patterns.

Despite its limitations, HDEMG remains a valuable tool for investigating neuromuscular function, offering high temporal resolution and the capacity for non-invasive, longitudinal monitoring of MU behavior. These features make it particularly well-suited for monitoring disease progression and evaluating therapeutic interventions, highlighting its potential as a translational tool in clinical and research settings.

6 Conclusions

The collective findings from these studies highlight the unique value of HDEMG in advancing our understanding of neuromuscular function, particularly in the context of torque estimation, corticospinal interactions, and neuromuscular disorders. By leveraging MU decomposition, HDEMG allows for a more detailed and physiologically meaningful characterization of MN behavior, moving beyond traditional muscle-level analyses. Across multiple applications, HDEMG has proven to be a powerful tool for investigating neural drive, muscle activation patterns, and neuromuscular adaptations due to injury or disease. Whether applied to torque estimation, the analysis of corticomuscular coupling, or the identification of neural adaptations in clinical populations, HDEMG offers a unique non-invasive interface to MN level control of muscle function.

One of the key strengths of HDEMG is its ability to capture neuromuscular adaptations across multiple levels, ranging from individual MUs to whole-muscle activity. This multi-scale resolution enables the simultaneous observation of traditional EMG parameters, such as amplitude and frequency content, alongside MU-level features including recruitment thresholds, discharge rates, and synchronization patterns. For instance, in stroke or SCI, HDEMG can detect altered MU recruitment, synchronization, and firing patterns, offering insights into neuroplastic changes associated with recovery or rehabilitation. Similarly, in applied fields such as biomechanics and assistive technologies, HDEMG-driven torque estimation provides a more physiologically grounded approach alternative to conventional amplitude-based EMG metrics, improving the accuracy and robustness of real-time control applications for prosthetics, exoskeletons, and rehabilitation devices. By capturing both aggregate muscle activation and the behavior of individual MUs,

HDEMG offers a comprehensive view of neuromuscular function across multiple levels of the motor pathway.

While HDEMG has clear advantages, its limitations must also be considered. MU decomposition is computationally demanding and requires careful validation, especially in pathological conditions where MU behavior may vary greatly between subjects and conditions. Additionally, the surface nature of HDEMG restricts its applicability to superficial muscles, limiting its applicability to deeper musculature. Nevertheless, many of these challenges can be addressed by integrating HDEMG with complementary techniques – such as EEG, neurostimulation, and computational modeling. These multi-modality approaches can enhance the interpretability of HDEMG data and provide a more comprehensive view of neuromuscular function.

Looking ahead, future research should prioritize the refinement of signal processing techniques, improving in the automation, reliability and the robustness of MU identification, and the expansion of HDEMG applications in clinical and translational settings. Ultimately, HDEMG stands a vital tool in neuromuscular research, bridging the gap between neural control and mechanical output and advancing both fundamental and applied contexts, such as rehabilitation and assistive devices.

Acknowledgments

I would like to sincerely thank everyone who has supported me throughout these years.

First and foremost, I am deeply grateful to my thesis supervisor, Assoc. Prof. Ruoli Wang, for her invaluable guidance, encouragement, and support throughout this research journey. Your expertise, patience, and understanding were essential in helping me complete this work. I would also like to express my gratitude to my thesis co-supervisor, Prof. Lanie Gutierrez-Farewik, for her insightful contributions to this research. Your sharp feedback and suggestions were incredibly helpful in shaping this project.

A big thank you to my co-authors for their contributions to the studies presented in this thesis. Special thanks to Zhihao Duan for all the technical support during both data collection and processing; to Olga Tarassova and Toni Arndt for their help and patience with data collection at GIH; to Emelie Butler Forslund for her guidance and active involvement from the very beginning to the completion of Study III; and to Xiaoling Hu, Hanxun Zhang, and Legeng Lin for their scientific insights and warm welcome in Hong Kong.

I would also like to extend my thanks to all my colleagues at the MoveAbility Lab for their support and camaraderie over these years. A special thank you to Antea for your help with data collection and company. Israel, Zhongzheng and Xiaochen, it was a pleasure to share an office with you.

Lastly, my warmest thanks to all the Bra Bra Family who supported me throughout these years. And to my dear Mauricio, this would not have been possible without you!

References

1. Socialstyrenlsen. The national board of health and welfare. *Statistics on Stroke 2023*. 2024, Official Statistics of Sweden.
2. Josefson, C., T. Rekand, A. Lundgren-Nilsson, and K.S. Sunnerhagen, *Epidemiology of Spinal Cord Injury in Adults in Sweden, 2016-2020: A Retrospective Registry-Based Study*. Neuroepidemiology, 2024: p. 1-9.
3. George, J.A., A.J. Gunnell, D. Archangeli, G. Hunt, M. Ishmael, K.B. Foreman, and T. Lenzi, *Robust Torque Predictions From Electromyography Across Multiple Levels of Active Exoskeleton Assistance Despite Non-linear Reorganization of Locomotor Output*. Front Neurorobot, 2021. **15**: p. 700823.
4. Cavallaro, E.E., J. Rosen, J.C. Perry, and S. Burns, *Real-time myoprocessors for a neural controlled powered exoskeleton arm*. IEEE Trans Biomed Eng, 2006. **53**(11): p. 2387-96.
5. Lyu, M., W.H. Chen, X. Ding, J. Wang, Z. Pei, and B. Zhang, *Development of an EMG-Controlled Knee Exoskeleton to Assist Home Rehabilitation in a Game Context*. Front Neurorobot, 2019. **13**: p. 67.
6. Wang, R., L. Zhang, H. Jalo, O. Tarassova, G.V. Pennati, and A. Arndt, *Individualized muscle architecture and contractile properties of ankle plantarflexors and dorsiflexors in post-stroke individuals*. Front Bioeng Biotechnol, 2024. **12**: p. 1453604.
7. Pizzolato, C., D.G. Lloyd, M. Sartori, E. Ceseracciu, T.F. Besier, B.J. Fregly, and M. Reggiani, *CEINMS: A toolbox to investigate the influence of different neural control solutions on the prediction of*

muscle excitation and joint moments during dynamic motor tasks. J Biomech, 2015. **48**(14): p. 3929-36.

8. Holobar, A., M.A. Minetto, and D. Farina, *Accurate identification of motor unit discharge patterns from high-density surface EMG and validation with a novel signal-based performance metric*. J Neural Eng, 2014. **11**(1): p. 016008.
9. Chen, C., S. Ma, X. Sheng, D. Farina, and X. Zhu, *Adaptive Real-Time Identification of Motor Unit Discharges From Non-Stationary High-Density Surface Electromyographic Signals*. IEEE Trans Biomed Eng, 2020. **67**(12): p. 3501-3509.
10. Hamill, J., Knutzen, K. M. & Derrick, T. R., *Biomechanical Basis of Human Movement, International Edition*. 4th ed. 2014: Lippincott Williams and Wilkins.
11. Kizyte, A., *High-Density Electromyography-Based Methods for Joint Torque Prediction and Motor Unit Behavior Observation*, in *Engineering Mechanics*. 2023, KTH Royal Institute of Technology: Stockholm, Sweden.
12. Anderson, D.E., M.L. Madigan, and M.A. Nussbaum, *Maximum voluntary joint torque as a function of joint angle and angular velocity: model development and application to the lower limb*. J Biomech, 2007. **40**(14): p. 3105-13.
13. Hill, A.V., *The heat of shortening and the dynamic constants of muscle*. Proceedings of the Royal Society of London. Series B - Biological Sciences, 1997. **126**(843): p. 136-195.
14. Kandel ER, S.J., Jessell TM, Siegelbaum SA, Hudspeth AJ, Mack S., *Principles of Neural Science, Fifth Edition*. 2014, New York, NY: McGraw-Hill Education.
15. Merletti, R.F., D., *Surface Electromyography: Physiology, Engineering, and Applications*. 2016, Hoboken, New Jersey: John Wiley Sons, Inc.
16. Challis, J.H. and J.H. Challis, *Electromyography*. Experimental Methods in Biomechanics, 2021: p. 69-80.
17. Henneman, E., G. Somjen, and D.O. Carpenter, *Functional Significance of Cell Size in Spinal Motoneurons*. J Neurophysiol, 1965. **28**: p. 560-80.
18. Milner-Brown, H.S., R.B. Stein, and R. Yemm, *The orderly recruitment of human motor units during voluntary isometric contractions*. J Physiol, 1973. **230**(2): p. 359-70.
19. Milner-Brown, H.S., R.B. Stein, and R. Yemm, *Changes in firing rate of human motor units during linearly changing voluntary contractions*. J Physiol, 1973. **230**(2): p. 371-90.

20. Baker, S.N., *Oscillatory interactions between sensorimotor cortex and the periphery*. Curr Opin Neurobiol, 2007. **17**(6): p. 649-55.

21. Gwin, J.T. and D.P. Ferris, *An EEG-based study of discrete isometric and isotonic human lower limb muscle contractions*. J Neuroeng Rehabil, 2012. **9**: p. 35.

22. Witte, M., L. Patino, A. Andrykiewicz, M.C. Hepp-Reymond, and R. Kristeva, *Modulation of human corticomuscular beta-range coherence with low-level static forces*. Eur J Neurosci, 2007. **26**(12): p. 3564-70.

23. Latash, M.L., *Methods in motor control studies*, in *Fundamentals of Motor Control*. 2012. p. 285-321.

24. Staudenmann, D., I. Kingma, A. Daffertshofer, D.F. Stegeman, and J.H. van Dieen, *Improving EMG-based muscle force estimation by using a high-density EMG grid and principal component analysis*. IEEE Trans Biomed Eng, 2006. **53**(4): p. 712-9.

25. Amer, N.S. and S.B. Belhaouari, *EEG Signal Processing for Medical Diagnosis, Healthcare, and Monitoring: A Comprehensive Review*. IEEE Access, 2023. **11**: p. 143116-143142.

26. Muceli, S. and R. Merletti, *Tutorial. Frequency analysis of the surface EMG signal: Best practices*. J Electromyogr Kinesiol, 2024. **79**: p. 102937.

27. Carvalho, C.R., J.M. Fernandez, A.J. Del-Ama, F. Oliveira Barroso, and J.C. Moreno, *Review of electromyography onset detection methods for real-time control of robotic exoskeletons*. J Neuroeng Rehabil, 2023. **20**(1): p. 141.

28. Brigham, E.O. and R.E. Morrow, *The fast Fourier transform*. IEEE Spectrum, 1967. **4**(12): p. 63-70.

29. Welch, P., *The use of fast Fourier transform for the estimation of power spectra: A method based on time averaging over short, modified periodograms*. IEEE Transactions on Audio and Electroacoustics, 1967. **15**(2): p. 70-73.

30. Kleine, B.U., J.P. van Dijk, B.G. Lapatki, M.J. Zwarts, and D.F. Stegeman, *Using two-dimensional spatial information in decomposition of surface EMG signals*. J Electromyogr Kinesiol, 2007. **17**(5): p. 535-48.

31. Gazzoni, M., D. Farina, and R. Merletti, *A new method for the extraction and classification of single motor unit action potentials from surface EMG signals*. J Neurosci Methods, 2004. **136**(2): p. 165-77.

32. Holobar, A. and D. Zazula, *Multichannel Blind Source Separation Using Convolution Kernel Compensation*. IEEE Transactions on Signal Processing, 2007. **55**(9): p. 4487-4496.

33. Holobar, A. and D. Farina, *Blind source identification from the multichannel surface electromyogram*. Physiol Meas, 2014. **35**(7): p. R143-65.

34. Holobar, A., V. Glaser, J.A. Gallego, J.L. Dideriksen, and D. Farina, *Non-invasive characterization of motor unit behaviour in pathological tremor*. J Neural Eng, 2012. **9**(5): p. 056011.

35. Li, X., A. Holobar, M. Gazzoni, R. Merletti, W.Z. Rymer, and P. Zhou, *Examination of Poststroke Alteration in Motor Unit Firing Behavior Using High-Density Surface EMG Decomposition*. IEEE Trans Biomed Eng, 2015. **62**(5): p. 1242-52.

36. Gogeascoechea, A., A. Kuck, E. van Asseldonk, F. Negro, J.R. Buitenweg, U.S. Yavuz, and M. Sartori, *Interfacing With Alpha Motor Neurons in Spinal Cord Injury Patients Receiving Trans-spinal Electrical Stimulation*. Front Neurol, 2020. **11**: p. 493.

37. Negro, F., S. Muceli, A.M. Castronovo, A. Holobar, and D. Farina, *Multi-channel intramuscular and surface EMG decomposition by convolutive blind source separation*. J Neural Eng, 2016. **13**(2): p. 026027.

38. Zhao, H., X. Zhang, M. Chen, and P. Zhou, *Adaptive Online Decomposition of Surface EMG Using Progressive FastICA Peel-Off*. IEEE Trans Biomed Eng, 2024. **71**(4): p. 1257-1268.

39. Mendez Guerra, I., D.Y. Barsakcioglu, and D. Farina, *Adaptive EMG decomposition in dynamic conditions based on online learning metrics with tunable hyperparameters*. J Neural Eng, 2024. **21**(4).

40. Wilson, J.M., C.K. Thompson, L.M. McPherson, C. Zadikoff, C.J. Heckman, and C.D. MacKinnon, *Motor Unit Discharge Variability Is Increased in Mild-To-Moderate Parkinson's Disease*. Front Neurol, 2020. **11**: p. 477.

41. Zijdewind, I. and C.K. Thomas, *Motor unit firing during and after voluntary contractions of human thenar muscles weakened by spinal cord injury*. J Neurophysiol, 2003. **89**(4): p. 2065-71.

42. Del Vecchio, A., F. Negro, A. Holobar, A. Casolo, J.P. Folland, F. Felici, and D. Farina, *You are as fast as your motor neurons: speed of recruitment and maximal discharge of motor neurons determine the maximal rate of force development in humans*. J Physiol, 2019. **597**(9): p. 2445-2456.

43. Coelli, S., A. Calcagno, C.M. Cassani, F. Temporiti, P. Reali, R. Gatti, M. Galli, and A.M. Bianchi, *Selecting methods for a modular EEG pre-processing pipeline: An objective comparison*. Biomedical Signal Processing and Control, 2024. **90**.

44. Halliday, D.M., J.R. Rosenberg, A.M. Amjad, P. Breeze, B.A. Conway, and S.F. Farmer, *A framework for the analysis of mixed time series/point process data--theory and application to the study of*

physiological tremor, single motor unit discharges and electromyograms. Prog Biophys Mol Biol, 1995. **64**(2-3): p. 237-78.

45. Liu, J., Y. Sheng, and H. Liu, *Corticomuscular Coherence and Its Applications: A Review*. Front Hum Neurosci, 2019. **13**: p. 100.

46. Negro, F., U.S. Yavuz, and D. Farina, *The human motor neuron pools receive a dominant slow-varying common synaptic input*. J Physiol, 2016. **594**(19): p. 5491-505.

47. Gao, Z., S. Lv, X. Ran, Y. Wang, M. Xia, J. Wang, M. Qiu, Y. Wei, Z. Shao, Z. Zhao, Y. Zhang, X. Zhou, and Y. Yu, *Influencing factors of corticomuscular coherence in stroke patients*. Front Hum Neurosci, 2024. **18**: p. 1354332.

48. Zipser-Mohammadzada, F., B.A. Conway, D.M. Halliday, C.M. Zipser, C.A. Easthope, A. Curt, and M. Schubert, *Intramuscular coherence during challenging walking in incomplete spinal cord injury: Reduced high-frequency coherence reflects impaired supra-spinal control*. Front Hum Neurosci, 2022. **16**: p. 927704.

49. Zhou, S., Z. Guo, K. Wong, H. Zhu, Y. Huang, X. Hu, and Y.P. Zheng, *Pathway-specific cortico-muscular coherence in proximal-to-distal compensation during fine motor control of finger extension after stroke*. J Neural Eng, 2021. **18**(5).

50. Hodgkin, A.L. and A.F. Huxley, *A quantitative description of membrane current and its application to conduction and excitation in nerve*. J Physiol, 1952. **117**(4): p. 500-44.

51. Abbott, L.F., *Lapicque's introduction of the integrate-and-fire model neuron (1907)*. Brain Res Bull, 1999. **50**(5-6): p. 303-4.

52. Caillet, A.H., A.T.M. Phillips, L. Modenese, and D. Farina, *NeuroMechanics: Electrophysiological and computational methods to accurately estimate the neural drive to muscles in humans in vivo*. J Electromyogr Kinesiol, 2024. **76**: p. 102873.

53. Ornelas-Kobayashi, R., A. Gogeascoechea, and M. Sartori, *Person-specific biophysical modelling of alpha-motoneuron pools driven by in vivo decoded neural synaptic input*. IEEE Trans Neural Syst Rehabil Eng, 2023. **PP**.

54. Ornelas-Kobayashi, R., I. Gomez-Orozco, A. Gogeascoechea, E. Van Asseldonk, and M. Sartori, *Personalized Alpha-Motoneuron Pool Models Driven by Neural Data Encode the Mechanisms Controlling Rate of Force Development*. IEEE Trans Neural Syst Rehabil Eng, 2024. **32**: p. 3699-3709.

55. Caillet, A.H., A.T.M. Phillips, D. Farina, and L. Modenese, *Estimation of the firing behaviour of a complete motoneuron pool by combining electromyography signal decomposition and realistic motoneuron modelling*. PLoS Comput Biol, 2022. **18**(9): p. e1010556.

56. Rossant, C., D.F. Goodman, J. Platkiewicz, and R. Brette, *Automatic fitting of spiking neuron models to electrophysiological recordings*. Front Neuroinform, 2010. **4**: p. 2.

57. Kramer, P.A., E.M. Feuerriegel, S.G. Lautzenheiser, and A.D. Sylvester, *Sensitivity of musculoskeletal models to variation in muscle architecture parameters*. Evol Hum Sci, 2022. **4**: p. e6.

58. Ao, D., G. Li, M.S. Shourijeh, C. Patten, and B.J. Fregly, *EMG-Driven Musculoskeletal Model Calibration With Wrapping Surface Personalization*. IEEE Trans Neural Syst Rehabil Eng, 2023. **31**: p. 4235-4244.

59. Serrancoli, G., A.L. Kinney, B.J. Fregly, and J.M. Font-Llagunes, *Neuromusculoskeletal Model Calibration Significantly Affects Predicted Knee Contact Forces for Walking*. J Biomech Eng, 2016. **138**(8): p. 0810011-08100111.

60. Zhang, L., D. Soselia, R. Wang, and E.M. Gutierrez-Farewik, *Lower-Limb Joint Torque Prediction Using LSTM Neural Networks and Transfer Learning*. IEEE Trans Neural Syst Rehabil Eng, 2022. **30**: p. 600-609.

61. Xiang, L., Y. Gu, Z. Gao, P. Yu, V. Shim, A. Wang, and J. Fernandez, *Integrating an LSTM framework for predicting ankle joint biomechanics during gait using inertial sensors*. Comput Biol Med, 2024. **170**: p. 108016.

62. Seth, A., M. Sherman, J.A. Reinbolt, and S.L. Delp, *OpenSim: a musculoskeletal modeling and simulation framework for in silico investigations and exchange*. Procedia IUTAM, 2011. **2**: p. 212-232.

63. Manal, K. and T.S. Buchanan, *A one-parameter neural activation to muscle activation model: estimating isometric joint moments from electromyograms*. J Biomech, 2003. **36**(8): p. 1197-202.

64. Lloyd, D.G. and T.F. Besier, *An EMG-driven musculoskeletal model to estimate muscle forces and knee joint moments in vivo*. J Biomech, 2003. **36**(6): p. 765-76.

65. Buchanan, T.S., D.G. Lloyd, K. Manal, and T.F. Besier, *Neuromusculoskeletal modeling: estimation of muscle forces and joint moments and movements from measurements of neural command*. J Appl Biomech, 2004. **20**(4): p. 367-95.

66. Millard, M., T. Uchida, A. Seth, and S.L. Delp, *Flexing computational muscle: modeling and simulation of musculotendon dynamics*. J Biomech Eng, 2013. **135**(2): p. 021005.

67. Al-Ayyad, M., H.A. Owida, R. De Fazio, B. Al-Naami, and P. Visconti, *Electromyography Monitoring Systems in Rehabilitation: A Review of Clinical Applications, Wearable Devices and Signal Acquisition Methodologies*. Electronics, 2023. **12**(7).

68. Cisnal, A., P. Gordaliza, J. Perez Turiel, and J.C. Fraile, *Interaction with a Hand Rehabilitation Exoskeleton in EMG-Driven Bilateral Therapy: Influence of Visual Biofeedback on the Users' Performance*. Sensors (Basel), 2023. **23**(4).

69. Sartori, M., D.G. Llyod, and D. Farina, *Neural Data-Driven Musculoskeletal Modeling for Personalized Neurorehabilitation Technologies*. IEEE Trans Biomed Eng, 2016. **63**(5): p. 879-893.

70. Sartori, M., U.S. Yavuz, and D. Farina, *In Vivo Neuromechanics: Decoding Causal Motor Neuron Behavior with Resulting Musculoskeletal Function*. Sci Rep, 2017. **7**(1): p. 13465.

71. Farina, D., R. Merletti, and R.M. Enoka, *The extraction of neural strategies from the surface EMG: 2004-2024*. J Appl Physiol (1985), 2025. **138**(1): p. 121-135.

72. Caillet, A.H., A.T.M. Phillips, D. Farina, and L. Modenese, *Motoneuron-driven computational muscle modelling with motor unit resolution and subject-specific musculoskeletal anatomy*. PLoS Comput Biol, 2023. **19**(12): p. e1011606.

73. Challis, J.H., *Electromyography*, in *Experimental Methods in Biomechanic*. 2020, Springer International Publishing. p. 69 - 80.

74. Zhang, L., Z. Li, Y. Hu, C. Smith, E.M.G. Farewik, and R. Wang, *Ankle Joint Torque Estimation Using an EMG-Driven Neuromusculoskeletal Model and an Artificial Neural Network Model*. IEEE Transactions on Automation Science and Engineering, 2021. **18**(2): p. 564-573.

75. Schulte, R.V., M. Zondag, J.H. Buurke, and E.C. Prinsen, *Multi-Day EMG-Based Knee Joint Torque Estimation Using Hybrid Neuromusculoskeletal Modelling and Convolutional Neural Networks*. Front Robot AI, 2022. **9**: p. 869476.

76. Wang, M., Z. Chen, H. Zhan, J. Zhang, X. Wu, D. Jiang, and Q. Guo, *Lower Limb Joint Torque Prediction Using Long Short-Term Memory Network and Gaussian Process Regression*. Sensors (Basel), 2023. **23**(23).

77. Hajian, G., E. Morin, and A. Etemad, *Convolutional Neural Network Approach for Elbow Torque Estimation during Quasi-dynamic and Dynamic Contractions*. Annu Int Conf IEEE Eng Med Biol Soc, 2021. **2021**: p. 665-668.

78. Ziai, A. and C. Menon, *Comparison of regression models for estimation of isometric wrist joint torques using surface electromyography*. J Neuroeng Rehabil, 2011. **8**: p. 56.

79. Yang, D., J. Zhao, Y. Gu, L. Jiang, and H. Liu, *EMG pattern recognition and grasping force estimation: Improvement to the myocontrol of multi-DOF prosthetic hands*, in *2009 IEEE/RSJ International Conference on Intelligent Robots and Systems*. 2009. p. 516-521.

80. Xu, L., X. Chen, S. Cao, X. Zhang, and X. Chen, *Feasibility Study of Advanced Neural Networks Applied to sEMG-Based Force Estimation*. Sensors (Basel), 2018. **18**(10).

81. Naik, G.R., S.E. Selvan, M. Gobbo, A. Acharyya, and H.T. Nguyen, *Principal Component Analysis Applied to Surface Electromyography: A Comprehensive Review*. IEEE Access, 2016. **4**: p. 4025-4037.

82. Hajian, G., A. Etemad, and E. Morin, *Automated Channel Selection in High-Density sEMG for Improved Force Estimation*. Sensors (Basel), 2020. **20**(17).

83. Abdi, H. and L.J. Williams, *Principal component analysis*. WIREs Computational Statistics, 2010. **2**(4): p. 433-459.

84. Awad, M. and R. Khanna, *Support Vector Regression*, in *Efficient Learning Machines*. 2015. p. 67-80.

85. Cao Xiao, J.S., *Introduction to deep learning for healthcare*. 2021: Springer.

86. Ian Goodfellow, Y.B., Aaron Courville, *Deep Learning*. 2016: MIT Press.

87. Perrouin-Verbe, B., C. Lefevre, P. Kieny, R. Gross, B. Reiss, and M. Le Fort, *Spinal cord injury: A multisystem physiological impairment/dysfunction*. Rev Neurol (Paris), 2021. **177**(5): p. 594-605.

88. Ditunno, J.F., Jr., M.E. Cohen, W.W. Hauck, A.B. Jackson, and M.L. Sipski, *Recovery of upper-extremity strength in complete and incomplete tetraplegia: a multicenter study*. Arch Phys Med Rehabil, 2000. **81**(4): p. 389-93.

89. Raineteau, O. and M.E. Schwab, *Plasticity of motor systems after incomplete spinal cord injury*. Nat Rev Neurosci, 2001. **2**(4): p. 263-73.

90. Gorgey, A.S. and G.A. Dudley, *Skeletal muscle atrophy and increased intramuscular fat after incomplete spinal cord injury*. Spinal Cord, 2007. **45**(4): p. 304-9.

91. Calancie, B., M.R. Molano, and J.G. Broton, *EMG for assessing the recovery of voluntary movement after acute spinal cord injury in man*. Clin Neurophysiol, 2004. **115**(8): p. 1748-59.

92. Calancie, B., M.R. Molano, J.G. Broton, J.A. Bean, and N. Alexeeva, *Relationship between EMG and muscle force after spinal cord injury*. J Spinal Cord Med, 2001. **24**(1): p. 19-25.

93. McKay, W.B., A.V. Ovechkin, T.W. Vitaz, D.G. Terson de Paleville, and S.J. Harkema, *Neurophysiological characterization of motor recovery in acute spinal cord injury*. Spinal Cord, 2011. **49**(3): p. 421-9.

94. Bravo-Esteban, E., J. Taylor, M. Aleixandre, C. Simon-Martinez, D. Torricelli, J.L. Pons, and J. Gomez-Soriano, *Tibialis Anterior muscle coherence during controlled voluntary activation in patients with*

spinal cord injury: diagnostic potential for muscle strength, gait and spasticity. J Neuroeng Rehabil, 2014. **11**: p. 23.

95. Keenan, K.G., W.V. Massey, T.J. Walters, and J.D. Collins, *Sensitivity of EMG-EMG coherence to detect the common oscillatory drive to hand muscles in young and older adults*. J Neurophysiol, 2012. **107**(10): p. 2866-75.

96. Neto, O.P. and E.A. Christou, *Rectification of the EMG signal impairs the identification of oscillatory input to the muscle*. J Neurophysiol, 2010. **103**(2): p. 1093-103.

97. Chen, M., Z. Lu, and P. Zhou, *A Dilemma for Coherence Calculation: Should Preprocessing Filters Be Applied?* Front Neurosci, 2022. **16**: p. 838627.

98. Xiong, G.X., J.W. Zhang, Y. Hong, Y. Guan, and H. Guan, *Motor unit number estimation of the tibialis anterior muscle in spinal cord injury*. Spinal Cord, 2008. **46**(10): p. 696-702.

99. Yang, J.F., R.B. Stein, J. Jhamandas, and T. Gordon, *Motor unit numbers and contractile properties after spinal cord injury*. Ann Neurol, 1990. **28**(4): p. 496-502.

100. Wiegner, A.W., M.M. Wierzbicka, L. Davies, and R.R. Young, *Discharge properties of single motor units in patients with spinal cord injuries*. Muscle Nerve, 1993. **16**(6): p. 661-71.

101. Ward, N.S. and L.G. Cohen, *Mechanisms underlying recovery of motor function after stroke*. Arch Neurol, 2004. **61**(12): p. 1844-8.

102. Zheng, Y., Y. Peng, G. Xu, L. Li, and J. Wang, *Using Corticomuscular Coherence to Reflect Function Recovery of Paretic Upper Limb after Stroke: A Case Study*. Front Neurol, 2017. **8**: p. 728.

103. Xu, R., H. Zhang, X. Shi, J. Liang, C. Wan, and D. Ming, *Lower-Limb Motor Assessment With Corticomuscular Coherence of Multiple Muscles During Ankle Dorsiflexion After Stroke*. IEEE Trans Neural Syst Rehabil Eng, 2023. **31**: p. 160-168.

104. Ushiyama, J., T. Suzuki, Y. Masakado, K. Hase, A. Kimura, M. Liu, and J. Ushiba, *Between-subject variance in the magnitude of corticomuscular coherence during tonic isometric contraction of the tibialis anterior muscle in healthy young adults*. J Neurophysiol, 2011. **106**(3): p. 1379-88.

105. Naros, G. and A. Gharabaghi, *Reinforcement learning of self-regulated beta-oscillations for motor restoration in chronic stroke*. Front Hum Neurosci, 2015. **9**: p. 391.

106. Bayraktaroglu, Z., K. von Carlowitz-Ghori, G. Curio, and V.V. Nikulin, *It is not all about phase: amplitude dynamics in corticomuscular interactions*. Neuroimage, 2013. **64**: p. 496-504.

107. Aikio, R., K. Laaksonen, V. Sairanen, E. Parkkonen, A. Abou Elseoud, J. Kujala, and N. Forss, *CMC is more than a measure of corticospinal tract integrity in acute stroke patients*. Neuroimage Clin, 2021. **32**: p. 102818.

108. Zheng, Y., B. Zheng, W. Qiang, Y. Peng, G. Xu, G. Wang, L. Li, and H. Shin, *Corticomuscular coherence existed at the single motor unit level*. Neuroimage, 2025. **305**: p. 120999.

109. Ibanez, J., A. Del Vecchio, J.C. Rothwell, S.N. Baker, and D. Farina, *Only the Fastest Corticospinal Fibers Contribute to beta Corticomuscular Coherence*. J Neurosci, 2021. **41**(22): p. 4867-4879.

110. Roberts, T.T., G.R. Leonard, and D.J. Cepela, *Classifications In Brief: American Spinal Injury Association (ASIA) Impairment Scale*. Clin Orthop Relat Res, 2017. **475**(5): p. 1499-1504.

111. Conable, K.M. and A.L. Rosner, *A narrative review of manual muscle testing and implications for muscle testing research*. J Chiropr Med, 2011. **10**(3): p. 157-65.

112. Meseguer-Henarejos, A.B., J. Sanchez-Meca, J.A. Lopez-Pina, and R. Carles-Hernandez, *Inter- and intra-rater reliability of the Modified Ashworth Scale: a systematic review and meta-analysis*. Eur J Phys Rehabil Med, 2018. **54**(4): p. 576-590.

113. Kumar, N., S. Nutakki, P. Patel, K.K. Lakhera, C. Sulaniya, A. Kumar, A. Babu, P. Singhal, B.S. Gora, and S. Singh, *Survival Trends Following Surgical Management in Carcinoma Vulva Patients During Covid 19 Pandemic: A Tertiary Care Hospital Study*. J Obstet Gynaecol India, 2024. **74**(6): p. 513-522.

114. Gladstone, D.J., C.J. Danells, and S.E. Black, *The fugl-meyer assessment of motor recovery after stroke: a critical review of its measurement properties*. Neurorehabil Neural Repair, 2002. **16**(3): p. 232-40.

115. Del Vecchio, A., A. Holobar, D. Falla, F. Felici, R.M. Enoka, and D. Farina, *Tutorial: Analysis of motor unit discharge characteristics from high-density surface EMG signals*. J Electromyogr Kinesiol, 2020. **53**: p. 102426.

116. Duan, Z., *In Vivo Estimation of Motor Unit Intrinsic Properties in Individuals with Spinal Cord Injury*, in *Engineering Mechanics*. 2025, KTH Royal Institute of Technology: Stockholm, Sweden.

117. Caillet, A.H., A.T.M. Phillips, D. Farina, and L. Modenese, *Mathematical relationships between spinal motoneuron properties*. Elife, 2022. **11**.

118. Seth, A., J.L. Hicks, T.K. Uchida, A. Habib, C.L. Dembia, J.J. Dunne, C.F. Ong, M.S. DeMers, A. Rajagopal, M. Millard, S.R. Hamner, E.M. Arnold, J.R. Yong, S.K. Lakshmikanth, M.A. Sherman, J.P. Ku, and S.L. Delp, *OpenSim: Simulating musculoskeletal dynamics and*

neuromuscular control to study human and animal movement. PLoS Comput Biol, 2018. **14**(7): p. e1006223.

119. Butler Forslund, E., M.T.N. Truong, R. Wang, A. Seiger, and E.M. Gutierrez-Farewik, *A Protocol for Comprehensive Analysis of Gait in Individuals with Incomplete Spinal Cord Injury*. Methods Protoc, 2024. **7**(3).

120. Martinez-Valdes, E., F. Negro, C.M. Laine, D. Falla, F. Mayer, and D. Farina, *Tracking motor units longitudinally across experimental sessions with high-density surface electromyography*. J Physiol, 2017. **595**(5): p. 1479-1496.

121. Oostenveld, R., P. Fries, E. Maris, and J.M. Schoffelen, *FieldTrip: Open source software for advanced analysis of MEG, EEG, and invasive electrophysiological data*. Comput Intell Neurosci, 2011. **2011**: p. 156869.

122. Taneja, K., X. He, Q. He, X. Zhao, Y.A. Lin, K.J. Loh, and J.S. Chen, *A Feature-Encoded Physics-Informed Parameter Identification Neural Network for Musculoskeletal Systems*. J Biomech Eng, 2022. **144**(12).

123. Ma, S., J. Zhang, C. Shi, P. Di, I.D. Robertson, and Z.Q. Zhang, *Physics-Informed Deep Learning for Muscle Force Prediction With Unlabeled sEMG Signals*. IEEE Trans Neural Syst Rehabil Eng, 2024. **32**: p. 1246-1256.

124. Williams, E.R. and S.N. Baker, *Circuits generating corticomuscular coherence investigated using a biophysically based computational model. I. Descending systems*. J Neurophysiol, 2009. **101**(1): p. 31-41.

125. Artoni, F., C. Fanciullacci, F. Bertolucci, A. Panarese, S. Makeig, S. Micera, and C. Chisari, *Unidirectional brain to muscle connectivity reveals motor cortex control of leg muscles during stereotyped walking*. Neuroimage, 2017. **159**: p. 403-416.

126. Gross, J., P.A. Tass, S. Salenius, R. Hari, H.J. Freund, and A. Schnitzler, *Cortico-muscular synchronization during isometric muscle contraction in humans as revealed by magnetoencephalography*. J Physiol, 2000. **527 Pt 3**(Pt 3): p. 623-31.